THESIS

INORGANIC GAS-AEROSOL PARTITIONING IN AND AROUND ANIMAL FEEDING OPERATION PLUMES IN NORTHEASTERN COLORADO IN LATE SUMMER 2021

Submitted by

En (Yuan) Li

Department of Atmospheric Science

In partial fulfillment of the requirements

For the Degree of Master of Science

Colorado State University

Fort Collins, Colorado

Fall 2023

Master's Committee:

Advisor: Jeffrey Pierce
Co-advisor: Emily Fischer

Shantanu Jathar
Amy Sullivan

Copyright by En (Yuan) Li 2023

All Rights Reserved

ABSTRACT

INORGANIC GAS-AEROSOL PARTITIONING IN AND AROUND ANIMAL FEEDING OPERATION PLUMES IN NORTHEASTERN COLORADO IN LATE SUMMER 2021

Ammonia (NH_3) from animal feeding operations (AFOs) is an important source of reactive nitrogen in the US, but despite its ramifications for air quality and ecosystem health, its near-source evolution remains understudied. To this end, Phase I of the Transport and Transformation of Ammonia (TRANS^{2}Am) field campaign was conducted in the northeastern Colorado Front Range in summer 2021 and characterized atmospheric composition downwind of AFOs during 10 research flights. Airborne measurements of NH_3, nitric acid (HNO_3), and a suite of water-soluble aerosol species collected onboard the University of Wyoming King Air (UWKA) research aircraft present a unique opportunity to investigate the sensitivity of particulate matter (PM) formation to AFO emissions. We couple the observations with thermodynamic modeling to predict the seasonality of ammonium nitrate (NH_4NO_3) formation. We find that during TRANS^{2}Am northeastern Colorado is consistently in the NH_3-rich and HNO_3-limited NH_4NO_3 formation regime. Further investigation using the Extended Aerosol Inorganics Model (E-AIM) reveals that summertime temperatures (mean: 23 ˚C) of northeastern Colorado, especially near the surface, inhibit NH_4NO_3 formation despite high NH_3 concentrations (max: ≤ 114 ppbv). Lastly, we model and winter conditions to explore the seasonality of NH_4NO_3 formation and find that cooler temperatures could support substantially more NH_4NO_3 formation. Whereas summertime NH_4NO_3 only exceeds 1 μg m^{-3} ~10% of the time in summer, modeled NH_4NO_3 would exceed 1 μg m^{-3}

61% (88%) of the time in spring/autumn (winter), with a 10˚C (20˚C) temperature decrease relative to the campaign.

ACKNOWLEDGMENTS

I would like to thank my collaborators, without whom this analysis would not be possible:

- Julieta Juncosa Calahorrano for helping me get acquainted to the dataset, model, and graduate school.
- Ilana Pollack and Rob Roscioli for their expertise in HNO_3 measurements.
- Dana Caulton, Megan McCabe, and the UWKA team for their help in data collection.
- Evelyn Bangs for her help in preparing and collecting the URG samples in Greeley, Colorado.
- Allie Mazurek and Marqi Rocque for providing daily forecasting for TRANS^{2}Am.

I would like to especially thank my committee members and advisors Amy Sullivan, Shantanu Jathar, Emliy Fischer, and Jeff Pierce for shaping this work with their expertise, curiosity, patience, and inspiring discussion.

This work was supported by the National Science Foundation (award # 2020127). Data from the TRANS2Am campaign used in this study can be found online at in the NCAR/UCAR EOL data archive: https://data.eol.ucar.edu/dataset/list?project=606&children=project.

Last but not least, I would thank my friends and family for their continuous and unwavering support.

TABLE OF CONTENTS

1 INTRODUCTION

Ammonia (NH_3) from agricultural activity accounts for over 80% of global emissions, with 50% from livestock manure and 30% from crop fertilizer (Wyer et al., 2022). Global NH_3 emissions and agricultural output have increased dramatically since the invention of the Haber-Bosch process in the early 20th century (Erisman et al., 2008; Galloway et al., 2004) and are projected to continue to increase in the near future to meet food security demands from a growing global population (Galloway et al., 2004; van Vuuren et al., 2011). The United States (US) is the third largest contributor of global NH_3 emissions (Liu et al., 2021). In the US, where NH_3 emissions remain unregulated, agriculture accounts for over 80% of domestic NH_3 emissions, with almost 50% of total domestic emissions attributable to livestock production (NEI, 2020).

Animal feeding operations (AFOs) are major agricultural point sources of NH_3. NH_3 hotspots from AFOs are large enough to be identified in satellite imagery (Van Damme et al., 2018) due to its short lifetime (hours-weeks) (Evangeliou et al., 2021; Juncosa Calahorrano et al., in press; Luo et al., 2022) and steep spatial gradients (e.g., Benedict et al., 2013). NH_3 from agricultural hotspots have also been shown to contribute significantly to nitrogen deposition in sensitive ecosystems (Benedict et al. 2018; Pan et al., 2021). AFOs emit NH_3 when nitrogen-containing compounds (e.g., urea and undigested proteins) in livestock waste volatilize (Behera et al., 2013; Wyer et al., 2022). The volatilization of NH_3 from AFOs is affected by waste management/storage practices and ambient conditions such as temperature, water content, wind speed, etc. (Behera et al., 2013; Hristov et al., 2011), with temperature being the most significant meteorological parameter (Robarg et al., 2002). Thus, NH_3 concentrations and AFO emissions generally peak in the summer (e.g., Eilerman et al., 2016; Wang et al. 2020).

Ammonia (NH_3) is the most abundant alkaline gas in the atmosphere and important for fine particulate matter ($PM_{2.5}$) formation. Under thermodynamically favorable conditions, gaseous NH_3 can partition to form aerosol phase ammonium (NH_4^+) and neutralize atmospheric acids such as sulfuric acid (H_2SO_4) and nitric acid (HNO_3) and contribute to a significant fraction of inorganic $PM_{2.5}$ (Jimenez et al., 2009). In the particle phase, NH_4^+ has adverse effects on (1) human health (Pope et al., 2009), (2) visibility (Hand et al., 2020), and (3) ecosystem health (via nitrogen deposition leading to soil acidification (Tian and Niu et al., 2015), and eutrophication (Zhan et al., 2017).

The inorganic gas-aerosol partitioning of NH_3-NH_4^+ is determined by complex, non-linear relationships between meteorological conditions and atmospheric composition. In the atmosphere, H_2SO_4 readily condenses into an acidic aerosol because of its low saturation vapor pressure (Ayers et al., 1980; Kulmala and Laaksonen, 1990; Roedel, 1979), and any NH_3 present will partition to the aerosol phase to form $(NH_4)_2SO_4$ until sulfate (SO_4^{2-}) is fully neutralized (Bassett and Seinfeld, 1983). After SO_4^{2-} is fully neutralized, excess NH_3 can react with HNO_3 to form NH_4NO_3 aerosols if thermodynamically favorable (Bassett and Seinfeld, 1983); therefore, HNO_3-NO_3 partitioning is also tightly coupled with NH_3-NH_4^+ partitioning. The gas-aerosol partitioning of the NH_3-HNO_3-NH_4NO_3 system is determined by the equilibrium constant K_p relative to the product of NH_3 and HNO_3, and NH_4NO_3 formation is thermodynamically favorable when the product of NH_3 and HNO_3 mixing ratios is supersaturated (i.e., $[NH_3][HNO_3] > K_p$). K_p is a function of temperature, and it is also a function of relative humidity (RH) for aqueous (as opposed to dry) aerosols. K_p is exponentially lower at lower temperatures (e.g., Stelson et al., 1967; Kim et al., 1993) and lower at higher RH for aqueous aerosols due to the inverse relationship between K_p and exponentially higher aerosol water content (AWC) (e.g., Russell et al., 1967; Basset and Seinfeld, 1983). The

gas-aerosol partitioning of the NH_3-HNO_3-NH_4NO_3 system is further complicated by interactions of NH_4^+ with other inorganic species such as non-volatile cations (NVCs; e.g., sodium [Na^+], potassium [K^+], calcium [Ca^{2+}], magnesium [Mg^{2+}]), organic acids (e.g., formate, oxalate, acetate), and nonpolar organic compounds (e.g., levoglucosan) (e.g., Metzger et al., 2006; Pun et al., 2002), so these complex gas-aerosol systems are studied using aerosol thermodynamic models.

Previous studies have used aerosol thermodynamic models to study inorganic gas-aerosol partitioning, including NH_4^+ formation, in various settings. Two common models are the Extended Aerosol Inorganics Model (E-AIM) (Clegg et al., 1998; Friese and Ebel, 2010) and ISORROPIA II (Fountoukis and Nenes, 2007). E-AIM is considered more accurate (Hennigan et al., 2015) and explicitly solves for thermodynamic equilibrium, with options to include Na^+ and Cl^- (Friese and Ebel, 2010) and organic acids and amines (Clegg et al., 2001). In contrast, ISORROPIA II trades accuracy for computational efficiency by making several approximations and includes Na^+, K^+, Mg^{2+}, Ca^{2+}, and Cl^- and an option to use precalculated activity coefficients for even faster calculations (Fountoukis and Nenes, 2007). Both of these models can calculate NH_3-NH_4^+ and HNO_3-NO_3^- partitioning either (1) as "closed-system" problems by using total (gas + aerosol) concentrations as inputs to predict the equilibrium-specific aerosol and gas concentrations or (2) as "open-system" problems by using aerosol concentrations as inputs to predict the equilibrium gas concentrations (Pye et al., 2020). Previous studies have shown that "open-system" problems are highly susceptible to error propagation from measurements (e.g., Fang et al., 2023; Hennigan et al., 2015; Murphy et al., 2017; Song et al., 2018); thus, both gas-phase measurements of NH_3 and HNO_3 and aerosol-phase measurements are required to accurately model NH_3-NH_4^+ and HNO_3-NO_3^- partitioning. There is a large body of work that has used weekly-to-hourly measurements of gas-phase and aerosol-phase species from surface monitoring sites to study

NH_3/NH_4^+ partitioning in various settings. For example, ISORROPIA II has been used to study the sensitivity of $PM_{2.5}$ to NH_3 and HNO_3 in urban and agricultural regions in the US, China, and Europe (Cheng et al., 2021; Guo et al., 2018; Nah et al., 2018) and the sensitivity of the vertical distribution of NH_3 to NH_4NO_3 partitioning at a suburban site in northeastern CO (Li et al., 2017). E-AIM has been used to study the sensitivity of urban $PM_{2.5}$ to NH_3-NH_4^+ (Tao and Murphy, 2019, 2021), amine vs. NH_3 uptake in marine $PM_{2.5}$ (Chen et al., 2022), and new approaches to estimating aerosol pH (Tao et al., 2022). However, Because of historic difficulties to measure NH_3 and HNO_3 at high temporal resolution with fast time responses (Roscioli et al., 2016; Pollack et al., 2019), application of these aerosol thermodynamic models to study NH_3-HNO_3-NH_4NO_3 partitioning in targeted agricultural NH_3 plumes at high sub-hour temporal resolution is lacking.

In comparison to surface monitoring sites, ground-based and airborne mobile sampling have the benefit of targeting NH_3 plumes from AFO outflow. Previous studies using ground-based mobile sampling have reported NH_3 and methane (CH_4) enhancement ratios from AFOs in northeastern Colorado (Eilerman et al., 2013) and the San Joaquin Valley in California (Miller et al., 2015). However, the inclusion of aerosol instrumentation in their payloads were restricted by space and power supply, and coverage was limited by speed and to roads. In contrast, airborne sampling provides better spatial and vertical coverage, but can share similar space/power limitations. Sorooshian et al. (2008) deployed a suite of instrumentation to characterize aerosols (e.g., composition, hygroscopicity, size distribution, etc.) downwind of an AFO but did not make any gas-phase measurements, so they could only infer whether NH_4NO_3 formation was NH_3- or HNO_3-limited. Staebler et al. (2009) measured NH_4^+, NO_3^-, SO_4^{2-}, and non-refractory organic aerosols and gaseous NH_3 (but not HNO_3) downwind of one AFO on three flights to study NH_3 loss processes. They found NH_3 loss to gas-aerosol partitioning was negligible (<4% NH_4^+:NH_x),

and dominated by advection (90%) and dry deposition (10%), on their three flights but did not utilize models to parse out which thermodynamic factors were inhibiting NH_4NO_3 formation. Hacker et al. (2016) tracked NH_3 and CH_4 enhancements downwind of AFOs on seven different flights, but could only measure NH_3 and CH_4 on alternating flights due to space/weight/power limitations of the two-seat motor glider. Schobesberger et al. (2023) measured NH_4^+, SO_4^{2-}, NO_3^-, and non-refractory organic aerosols and NH_3 to investigate the surface-atmosphere exchange of NH_3 and found net NH_3 flux from the surface to the atmosphere at an agricultural region; they also note that NH_3:NH_4^+ ratios are lower in the free troposphere compared to the boundary layer likely due the temperature-dependence of NH_3-NH_4^+ partitioning.

In a 2019 pilot study to the Transport and Transformation of Ammonia (TRANS^{2}Am) campaign, Pollack et al. (2022) used 1 Hz measurements of NH_3, CH_4, and ethane (C_2H_6) to isolate agricultural CH_4 from nearby oil and natural gas (ONG) CH_4 emissions and quantify NH_3:CH_4 enhancement ratios from 6 AFOs, and McCabe et al. (2023) used these measurements to compare two methods of calculating agricultural CH_4 emission rates in a region with co-located ONG activity and reported NH_3 and CH_4 fluxes from livestock. Building off of this pilot study, the full TRANS^{2}Am campaign was conducted in northeastern Colorado in July/August 2021 (Phase I) and August 2022 (Phase II) and included a more comprehensive payload with the addition of gas-phase HNO_3 and aerosol composition measurements. The TRANS^{2}Am campaign provides a unique dataset containing both gas and aerosol composition at high temporal resolution in and around agricultural NH_3 plumes, which can be used to quantify NH_3 emissions and study the near-source evolution and loss processes of NH_3 from AFOs (Juncosa Calahorrano et al., in press).

In this work, we use the comprehensive suite of observations from Phase I of TRANS^{2}Am in tandem with model analyses to investigate (1) the sensitivity of particulate matter (PM) formation to AFO emissions, and (2) the seasonality of NH_4NO_3 formation in northeastern Colorado. Section 2.1 outlines the TRANS^{2}Am field campaign, Section 2.2 describes the TRANS^{2}Am instrument payload, and Section 2.3 describes the aerosol thermodynamic model. Section 3.1 discusses the observed NH_4NO_3 thermodynamic regimes. Section 3.2 provides a discussion of model-observation comparisons and two case studies. Section 3.3 delves into the temperature-sensitivity of NH_4NO_3 partitioning during TRANS^{2}Am, and Section 3.4 explores the seasonality of NH_4NO_3 formation by modeling idealized scenarios beyond the summertime measurements.

2 METHODS

2.1 TRANS^{2}Am

The Transport and Transformation of Ammonia (TRANS^{2}Am) campaign deployed the University of Wyoming King Air (UWKA) over northeastern Colorado (Figure 1) during July/August 2021 (Phase I) and August 2022 (Phase II) to characterize the atmospheric composition downwind of AFOs and understand the chemical and physical evolution of NH_3. There were 24 research flights consisting of 17 near-source sampling flights, 6 upslope flights, and 1 satellite-underpass. Combined with a low-altitude waiver, this smaller research aircraft was able to routinely sample between 200 and 1000 ft AGL. Here we focus on the inorganic gas-aerosol partitioning during only the Phase I near-source sampling flights. Near-source sampling flights included circling facilities to manually identify the outflow direction, followed by vertically stacked boxes at multiple intervals downwind of targeted AFOs. Flights were generally flown on hot, dry afternoons when surface winds were strong (> 5 m s^{-1}) enough to form and identify well-defined NH_3 plumes. Smoke-impacted days accounted for 8 of the 10 near-source sampling flights during Phase I in 2021.

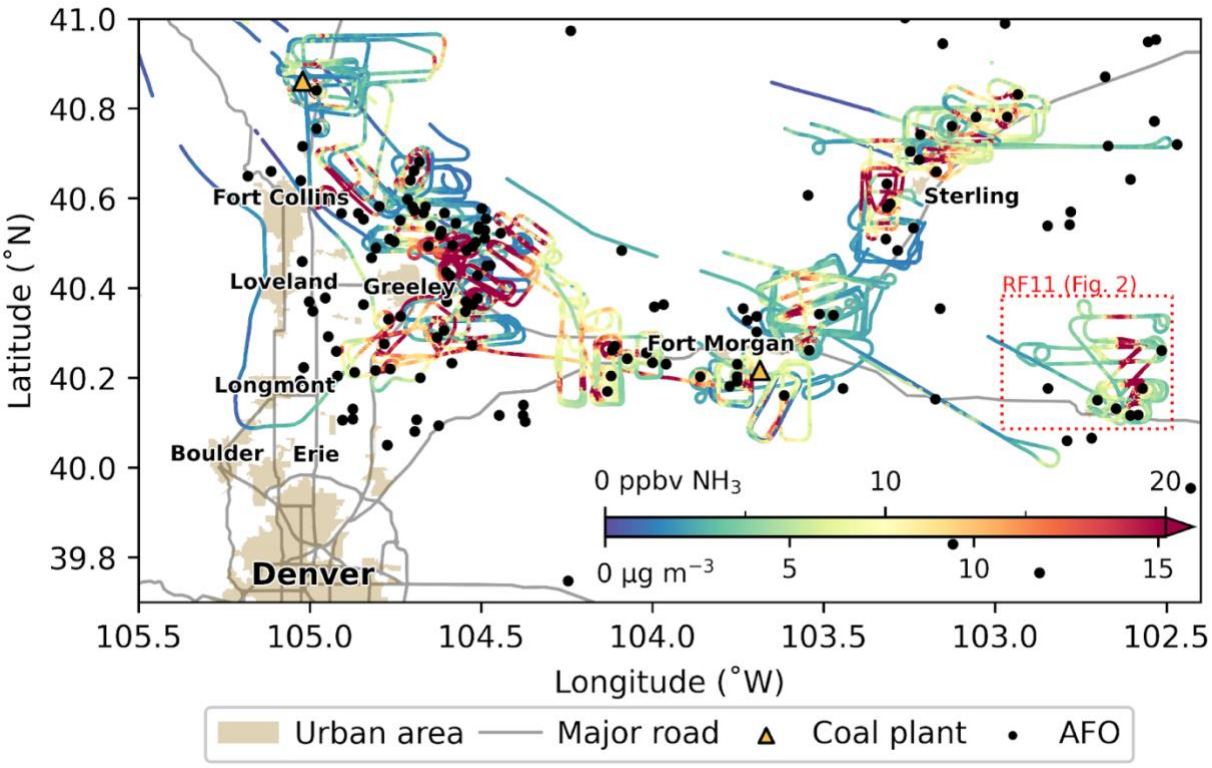

Figure 1. Map of near-source flights from TRANS^{2}Am Phase I (≤1500 m agl) colored by 1 Hz NH_3 concentration. The colorbar is truncated at 20 ppbv, and the maximum observed NH_3 concentration is > 400 ppbv. The red dotted line outlines RF11, which is plotted as a time series in Figure 2.

Figure 1 shows the study region including a large number of different types of AFOs (e.g., cattle, dairy, poultry, etc.), and urban areas along the major road corridor from Denver to Fort Collins. Active oil and gas operations in this region are depicted in Pollack et al. (2022). The study region is bordered by the Rocky Mountains on the west. We restrict the analysis to data collected below 1500 m agl and ≤ 41˚N. This removes data associated with takeoff/landing from the operations base at Laramie Regional Airport.

2.2. Aircraft Instrumentation

The UWKA instrument payload measured a suite of aerosol-phase and gas-phase species to study the inorganic gas-aerosol partitioning around AFO outflow. The full instrument payload

is described in detail in Juncosa Calahorrano et al. (in press), so here we describe the payload relevant to our study and summarize it in Table 1.

Table 1. Summary of UWKA instrument payload and measured parameters used in this work.

Parameter	**Instrument**	**Sampling Frequency**	**Limit of Detection**
Submicron Aerosol Composition NH_4^+ SO_4^{2-} NO_3^- NO_2^- Cl^- Na^+ K^+ Mg^{2+} Ca^{2+} Acetate CH_3COO^- Oxalate $C_2O_4^{2-}$ Formate $HCOO^-$ MSA* $CH_3SO_3^-$ Glutarate $C_5H_7O_4^-$ Propionate $C_3H_5O^{2-}$ Succinate $C_4H_4O_4^{2-}$ Levoglucosan $C_6H_{10}O_5$	PILS with Fraction Collector	2 minutes	0.001 µg m^{-3}
NH_3	QC-TILDAS operating at 967 cm^{-1}	1 second	180 pptv
HNO_3	QC-TILDAS operating at 1723 cm^{-1}	1 second	555 pptv

*Methanesulfonate (MSA)

Figure 2 shows an exemplary time series of the full suite of observations collected during a single research flight on August 17, 2021. The full suite of observations includes 9 inorganic species, 8 organic species, and gas-phase NH_3 and HNO_3. The details of this figure will be discussed more in the results section. The 2-minute averaged NH_3 masks much of the observed variability present in the 1-Hz observations. For instance, the reported maximum gas-phase NH_3 reported here (114 ppbv) corresponds to the 2-min average, whereas the maximum NH_3 sampled using the 1 Hz data is > 400 ppbv. Temperature, RH, and geospatial data are from the UWKA standard suite of instrumentation.

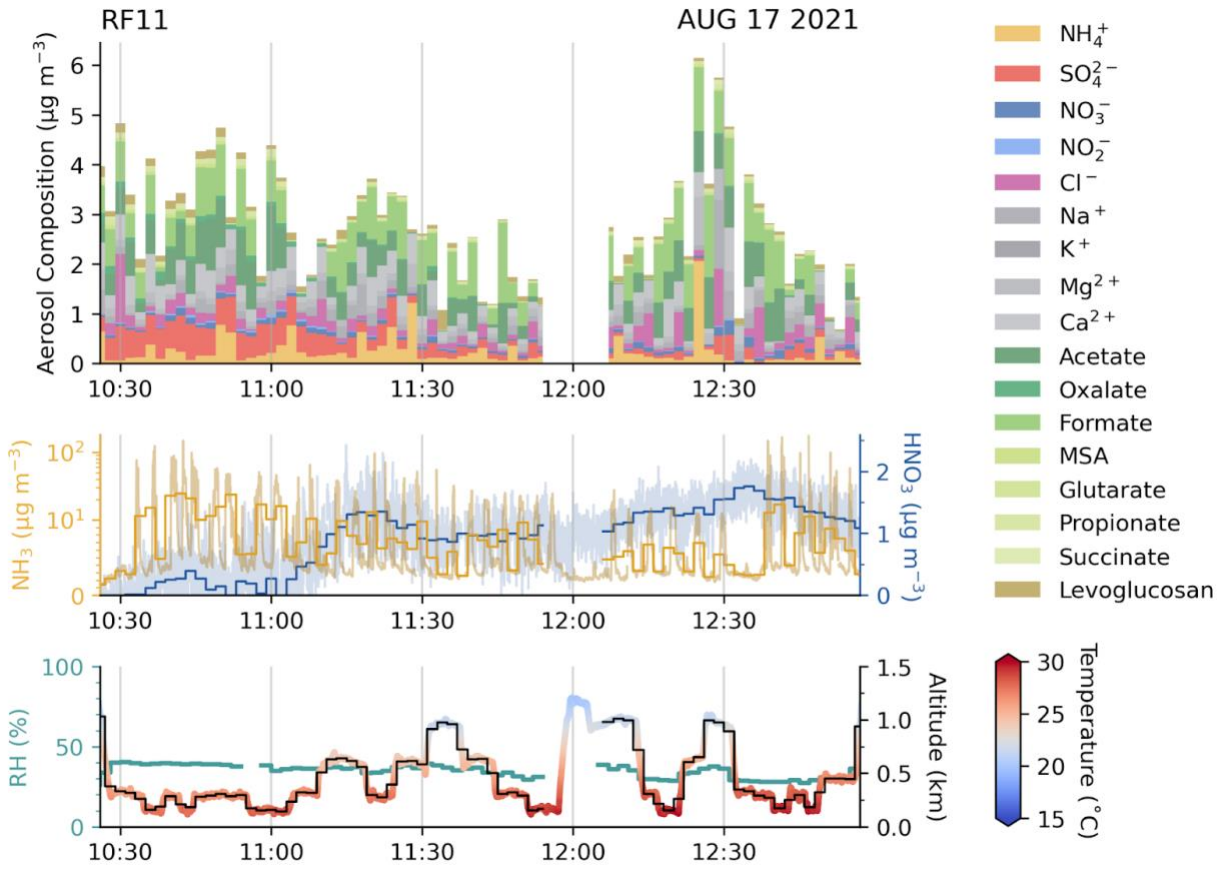

Figure 2. Time series of observations from RF11 in local time. The flight track from RF11 is outlined by the red dotted line in Figure 1 and the plane is flying vertically stacked boxes as it moves downwind of the target facility from ~10:30 to 12:30 before flying back south and circling the target facility again. Top: Aerosol-phase measurements colored by species. Middle: Gas-phase NH_3 in yellow (left y-axis) and HNO_3 in blue (right y-axis) averaged to 2-minute PILS timesteps. Light shade represents native 1 Hz measurements. Bottom: RH (left y-axis) and altitude colored by temperature (right y-axis). See Table S1 in supplementary information for summary statistics of each species.

Water-soluble aerosol samples were collected by a Particle-into-Liquid Sampler (PILS) with a fraction collector for offline analysis using ion chromatography. A PILS works by collecting ambient aerosol particles into pure water to produce a liquid sample with aerosol particles dissolved in it. The PILS sampled air at 15 LPM from the NCAR-University of Wyoming Aerosol Inlet mounted on top of the UWKA fuselage (Snider et al., 2018). A non-rotating MOUDI impactor stage upstream of the PILS removes super-micron particles to provide a size cutoff of 1 µm (PM_1) (Marple et al., 1991). Sodium-carbonate- and phosphorous-acid-coated denuders remove gaseous inference before the particles are mixed with hot steam to create a supersaturated environment (RH

≥ 100%) and grow the particles large enough to be collected by an impactor. The particles are then washed off the impactor by a continuous flow of deionized water providing the liquid sample with the dissolved aerosol particles for analysis (Orsini et al., 2003). Finally, the liquid sample is continuously collected by a Bretchel Fraction Collector for offline analysis (Sorooshian et al., 2006). The fraction collector holds seventy-two 2 mL polypropylene vials on a carousel, and the PILS liquid flow rate was set such that a ~1.2 mL liquid sample is collected into a vial every two minutes (Sullivan et al., 2022). Preloaded carousels were manually switched during each flight to allow for collection of samples across an entire flight. Background samples were also collected each flight for 10 minutes by forcing the airflow through a HEPA filter before entering the PILS. Immediately after each flight, the vials were unloaded, recapped with solid caps, and transported to Colorado State University in coolers with ice packs to be stored at 2˚C until analysis.

Offline analysis of PILS samples was performed by ion chromatography to determine the aerosol-phase concentrations of cations, anions/organic acids, and levoglucosan (full list of species measured provided in Table 1). Cations were determined using a Dionex ICS-3000 ion chromatography with a pump, conductivity detector, and self-regenerating cation suppressor. A Dionex IonPac CS12A analytical column (3 × 150 mm) using 20 mM methanesulfonic acid at a flow rate of 0.5 mL/min was used for the cation separation. The injection volume and analysis time were 190 µL and 17 minutes, respectively. Anions/organic acids were measured using a Dionex ICS-4000 capillary ion chromatograph. A Dionex AS11-HC capillary column with a potassium hydroxide gradient provided by an eluent generator at a flow rate of 0.015 mL/min was used for the separation. The complete run time was 65 min with an injection volume of 35 µL. Levoglucosan was determined via high-performance anion-exchange chromatography with pulsed amperometric detection (HPAEC-PAD) using a Dionex DX-500 series ion chromatograph with an

ED-50/ED-50A electrochemical cell. The cell includes two electrodes: a pH-Ag/AgCl (silver/silver chloride) reference electrode and "standard" gold working electrode. For the separation, a Dionex CarboPac PA-1 column (4×250 mm) employing a sodium hydroxide gradient was used. The complete run time was 59 min, and the injection volume was 100 µL. More details can be found in Sullivan et al. (2011a,b, 2014, 2019, 2022). Samples were blank-corrected using the average of all background samples collected on that particular flight. The uncertainty is ±10% and the limit of detection is 0.001 µg m^{-3} for all species.

NH_3 mixing ratios were measured using a closed-path quantum-cascade tunable infrared laser direct absorption spectrometer (QC-TILDAS) with an effective path length of 76 m and operating at 967 cm^{-1} (Ellis et al., 2010; McManus et al., 1995, 2010; Zahniser et al., 1995). The NH_3 QC-TILDAS is operated with a high sample flow rate (> 10 SLPM) to help prevent adsorption of NH_3 to the sampling surfaces. The instrument was also operated with a heated inertial inlet positioned along the flowpath to reduce (1) condensation of water (that NH_3 can dissolve in/adsorb to), (2) adsorption of NH_3 to the sampling surfaces, and (3) a positive bias from semivolatile ammonium particles > 300 nm in diameter (Ellis et al., 2010). The time response of the NH_3 QC-TILDAS has been previously characterized and defined as the time required for 90% signal recovery following a step change in NH_3 calibration signal (Pollack et al., 2019). During $TRANS^2Am$, a time response of 1-2 s could be maintained with regular cleaning of the instrument sampling surfaces between flights. The instrument was calibrated on the ground between flights and regularly zeroed in flight by overblowing the aircraft inlet with ultra-pure air. The flowpath was also copiously flushed with ultra-pure air following calibrations. The calibration source was a thermally-stabilized, certified NH_3 permeation device (Kin-Tek). The permeation rate of the calibration source was verified before and after the field study using the NOAA UV absorption

system and determined to have an uncertainty of ±10% (Neuman et al., 2003; Pollack et al., 2019). The instrument was also mounted on a vibrationally-isolated rack to minimize motion sensitivity in flight (Pollack et al., 2019). The 1-Hz precision of the instrument is 60 pptv; the detection limit is defined as 3 times the precision (180 pptv). NH_3 measurements are collected at 10 Hz and averaged to 1 Hz for reporting and further averaged to 2 minutes to match the PILS time resolution for this analysis. The uncertainty of NH_3 is ±12% of the measured mixing ratio (Pollack et al., 2019).

HNO_3 mixing ratios are measured using a separate closed-path QC-TILDAS with a 76 m pathlength and measuring absorption by the molecule at 1723 cm^{-1} (Roscioli et al., 2016). Owing to weight, space, and power available on the UWKA, the HNO_3 measurements were categorized as second priority for the TRANS^{2}Am payload. The only way the HNO_3 QC-TILDAS could be implemented aboard the aircraft was to share a common aircraft inlet, inertial inlet, and pumping system with the NH_3 instrument. Because of the shared flowpath, the same instrument operation practices are applied (e.g., regular in-flight zeros, calibrations on the ground between flights, regularly cleaning samping surfaces and inlet components, and copiously flushing the sample flow path with ultrapure air following individual NH_3 and HNO_3 calibrations). The HNO_3 QC-TILDAS is also mounted on vibration isolators in the aircraft equipment rack. The 1-Hz precision is 185 pptv resulting in a detection limit of 555 pptv. The uncertainty for the HNO_3 measurement is determined to be ±20% of the measured mixing ratio following the procedures in Pollack et al. (2019). When operated with a dedicated flowpath, the HNO_3 QC-TILDAS has been previously reported to have a 70 s time response for a 90% signal recovery (Roscioli et al., 2016). Even with the high sample flow rate (> 10 SLPM) and regular cleaning of the sampling surfaces, the 90% HNO_3 signal recovery time following a step change in HNO_3 calibration signal during ground

calibration days between flights during TRANS^{2}Am was closer to 500 s. The longer response time is likely related to the HNO_3 QC-TILDAS being positioned downstream of the NH_3 QC-TILDAS. There was a longer flow path between the inlet tip and the HNO_3 detector, and this pathway was susceptible to adsorption of HNO_3 on the sampling surfaces prior to detection. Owing to a larger detection limit and uncertainty in the HNO_3 measurement compared to NH_3, we consider the 1/*e* response time (which is closer to 200 s) to be a more representative time response for the HNO_3 measurement. For this work, and to match the sampling frequency of PILS, the HNO_3 measurements are averaged to 120 s prior to further analyses.

Active continuous passivation of the sampling surfaces has been shown to improve time response for closed-path QC-TILDAS instruments (Roscioli et al., 2016; Pollack et al., 2019). Prior work shows success in improving the time response of a single-channel, closed-path NH_3 QC-TILDAS when using a strong perfluorinated base as the passivant and for a separate HNO_3 QC-TILDAS when using a strong perfluorinated acid as the passivant (Roscioli et al., 2016; Pollack et al., 2019). However, active continuous passivation could not be implemented during TRANS^{2}Am owing to the common flow path for the payload configuration.

2.3 Model

The Extended Aerosol Inorganic Model (E-AIM) aerosol thermodynamic model was used to investigate factors driving the gas-aerosol partitioning of NH_3 and HNO_3. The E-AIM Model II (http://www.aim.env.uea.ac.uk/aim/aim.php) calculates the equilibrium phase partitioning of an inorganic H_2O-SO_4^{2-}-NO_3^--NH_4^+ aerosol system with an option to add preset and custom organic acids and amines. In this study, we add the three most abundant (di-)carboxylic acids–formic acid, oxalic acid, and acetic acid–to the default inorganic aerosol system with custom property files that include molar mass, dissociation constants, and UNIFAC (UNIQUAC Functional-group Activity

Coefficients, where UNIQUAC is a portmanteau of UNIversal QUAsiChemical) activity coefficients and restrict the organic compounds to the aqueous-phase. Given 11 other measured aerosol species, we conduct a comprehensive suite of sensitivity tests with different combinations of NVCs, Cl^-, levoglucosan, and a proxy for unmeasured smoke-related organic compounds (Figure S1), but find that they worsen model-observation agreement (see Figure S2 and Section 2 in SI for further discussion). The model inputs are measurements of temperature, relative humidity, total ammonia ($NH_x = NH_3 + NH_4^+$), and total nitrate ($TNO_3 = HNO_3 + NO_3^-$), as well as particle-phase sulfate, formate, acetate, and oxalate. We find that the inclusion of formate, oxalate, and acetate in the model help correct for NH_4^+ and NO_3^- underestimates by the model (Figure S1 panels a and b), and these three compounds have been observed to be the most abundant organic acids in aerosols (Nah et al., 2018). The primary model outputs used in our study are the gas-aerosol partitioning of total NH_x and TNO_3. Previous studies ran E-AIM and ISORROPIA II in metastable mode (e.g., Cheng et al., 2021; Guo et al., 2018; Nah et al., 2018; Tao et al., 2022; Tao and Murphy, 2019, 2021) because aqueous aerosol salts have been observed in the atmosphere below their deliquescence relative humidity (DRH) (Rood et al., 1989), so we also run the model in metastable mode such that aerosols may exist in the aqueous phase below their DRH. Therefore, to apply E-AIM to our analysis, we make a key assumption that the submicron aerosol population is internally mixed and at metastable equilibrium.

2.4 URG Measurements

We also include gas-phase HNO_3 and NH_3 measurements from a ground-based URG annular denuder/filter pack sampler located at the Weld County Tower site in Greeley, CO, which is operated by the Colorado Department of Public Health and Environment (CDPHE). Weekly samples were collected from mid-March through mid-October from 2014 to 2019 (excluding

2018). Ambient air was pulled into the sampler at a flow rate of 3 LPM through a $PM_{2.5}$ Teflon-coated cyclone followed by sodium carbonate and phosphorous acid coated denuders to collect gas-phase HNO_3 and NH_3 (Benedict et al., 2013a?). The air then passed through a 47 mm nylon filter to collect PM. Finally, the air passed through a second phosphorous acid denuder to collect any particulate NH_4^+ that volatilized off the filter (Yu et al., 2005).

Each nylon filter was extracted in 6 mL DI Water in a polystyrene test tube and sonicated without heat for 40 min. Each denuder was extracted in 10 mL DI Water. Both extracts were then analyzed for anion and cation species using ion chromatography. Both systems utilized a Dionex DX-500 IC, which includes an isocratic pump, self-regenerating anion or cation suppressor, and conductivity detector. The injection volume and analysis time of both methods was 50 µL and 17 minutes, respectively. The anions were quantified using a Dionex IonPac AS14A (4 × 150 mm) analytical column with a 1 mM sodium bicarbonate/8 mM sodium bicarbonate eluent at a flow rate of 1 mL/min. A Dionex IonPac CS12A (3 × 120 mm) analytical column was used with 20 mM methanesulfonic acid eluent at a flow rate of 0.5 mL/min.

3 RESULTS

3.1 Overview

Figure 1 shows that northeastern Colorado is characterized by high and spatially variable NH_3 concentrations. NH_3 concentrations have been shown to vary by orders of magnitude from tens of pptv over remote oceans to tens of ppbv in agricultural regions (Nair and Yu, 2020), and can exhibit steep spatial gradients within agricultural regions (Benedict et al., 2013). Li et al. (2017) reported weekly and biweekly averaged NH_3 concentrations at 14 surface monitoring sites in northeastern Colorado during summers 2010-2015 ranging from 4 ppbv (2.66 µg m^{-3}) over grasslands to 60 ppbv (42.7 µg m^{-3}) near AFOs. Due to the finer temporal resolution and the spatial and vertical variability of our airborne measurements, we capture higher concentrations (20 - 114 ppbv) in targeted AFO outflow and lower concentrations outside of plumes (0.5 - 20 ppbv). We found that NH_3 accounts for 93% of NH_x on average, and Day et al. (2012) also found that NH_x is dominantly in the gas-phase throughout the year in northeastern Colorado.

HNO_3 concentrations observed during TRANS^{2}Am demonstrate much less spatial and temporal variability than NH_3 concentrations. HNO_3 concentrations were 1.7 ppbv on average and varied from below LOD (555 pptv) to 4 ppbv, and accounted for about 94% of TNO_3 on average. We did not identify any spatial gradients of increasing HNO_3 concentrations towards urban areas, although the UWKA did not sample directly overhead urban areas.

For the species that the PILS resolves in this study, PM_1 concentrations were 4.8 µg m^{-3} on average (σ = 2.0 µg m^{-3}), with inorganic species accounting for 54% and organic species accounting for 45%. The observed inorganic PM_1 mass is dominated by sulfate (0.52 ± 0.37 µg m^{-3} [mean ± standard deviation]), nitrate (0.33 ± 0.48 µg m^{-3}) and ammonium (0.38 ± 0.54 µg m^{-3}).

The observed organic PM_1 mass is dominated by acetate (1.1 ± 0.7 µg m^{-3}), formate (0.72 ± 0.61 µg m^{-3}), and oxalate (0.14 ± 0.13 µg m^{-3}).

3.2 Observed Thermodynamic Regimes

Figure 3 shows that the thermodynamic regimes sampled during TRANS^{2}Am are always NH_3-rich and mostly HNO_3-limited. The thermodynamic regimes are determined by the gas ratio, which was introduced by Ansari and Pandis (1998) and is defined in molar concentrations:

The gas ratio is always positive, indicating that sulfate is always fully neutralized and that there is always sufficient NH_3 and HNO_3 to form NH_4NO_3. Only 6% (37/629) of sample air masses have a gas ratio between 0 and 1 where NH_4NO_3 formation is NH_3-limited; the remaining 94% (592/629) have a gas ratio greater than 1, where NH_4NO_3 formation is HNO_3-limited. NH_3-limited conditions are only measured when NH_3 is in the lowest 25th percentile (≤ 4.7 ppbv). These conditions only occur sporadically away from major sources. Even though summertime AFO outflow is largely HNO_3-limited, NH_4NO_3 formation can still be sensitive to NH_3 (see Section 3.4 for further discussion).

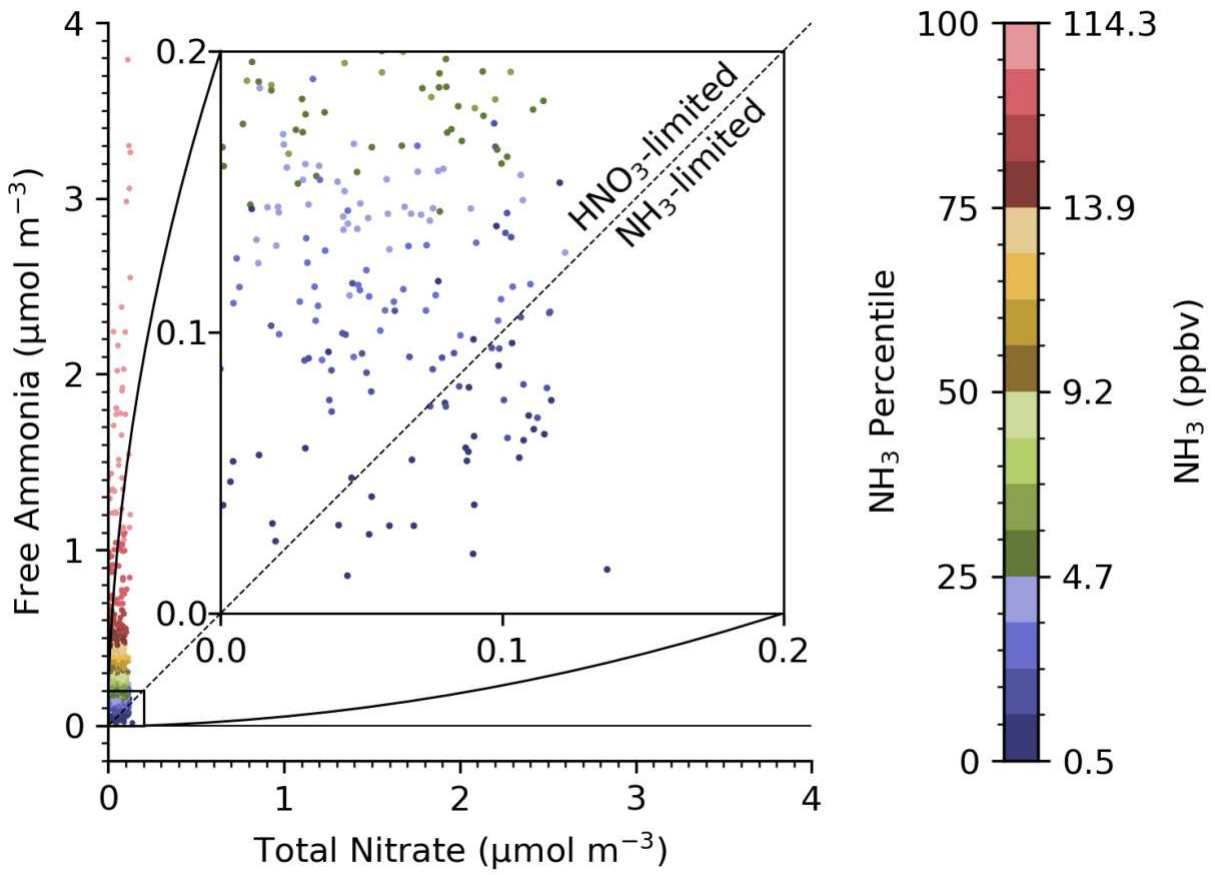

Figure 3. Molar concentrations of free ammonia (NH_3 + NH_4^+ - $2SO_4^{2-}$) vs. total nitrate (HNO_3 + NO_3^-). Colorbar represents NH_3 percentiles and respective concentrations in ppbv are given for quartiles. Inset axes are zoomed in to the range of observed total nitrate. The dashed line delineates NH_3- and HNO_3-limited NH_4NO_3 formation regimes.

3.3 Thermodynamic Modeling

Figure 4 shows the distribution of observed and modeled NH_4^+ and NO_3^- binned by altitude. We find that across the full campaign in aggregate, the E-AIM simulations capture the correct order of magnitude of the observed NH_4^+ and NO_3^- concentrations. Model and observations agree that there was generally little NH_4NO_3 formation, especially below 300 m. Below 300 m agl, NH_4^+ exceeds 1 µg m^{-3} only 2% of the time in observations and 0.3% of the time in the model, and NO_3^- exceeds 1 µg m^{-3} 4% of the time in observations and 3% of the time in the model. Summertime Colorado is hot and dry, both of which thermodynamically inhibit NH_4NO_3 formation and drive gas-aerosol partitioning into the gas-phase.

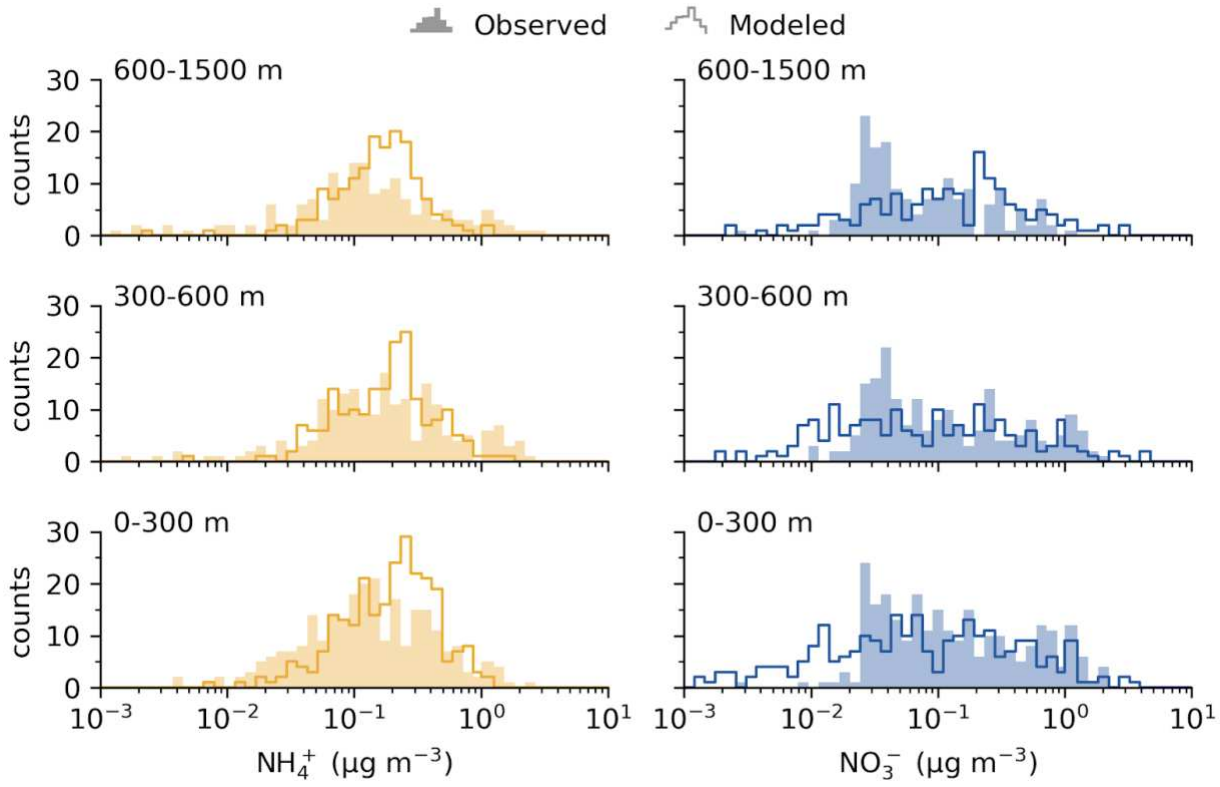

Figure 4. Distributions of observed (shaded region) and modeled (solid line) NH_4^+ (left) and NO_3^- (right) by altitude bins (rows) for the 10 near-source flights during TRANS^{2}Am Phase I.

A variance analysis reveals that above 0.5 μg m^{-3} NH_4^+ and NO_3^-, E-AIM systematically underpredicts NH_4^+ by ⅔ and NO_3^- by ½ (Figure S4 panels c and h). The model overpredicts NH_4^+ and NO_3^- under two different nonequilibrium conditions: (1) The model overpredicts NH_4^+ and NO_3^- at NH_3 concentrations > 50 ppbv (Figure S4 panels a and e), suggesting that the NH_3-HNO_3-NH_4NO_3 system in the sampled AFO plumes is supersaturated with NH_3 and has not yet reached equilibrium. This occurs only on one flight (RF13) which sampled the highest NH_3 concentrations by almost an order of magnitude (Figure S5). (2) The model also overpredicts NH_4^+ and NO_3^- when the plane ascends to cooler temperatures (< 20˚C) under dry (< 60% RH), high-HNO_3 (> 2 ppbv) conditions Figure S4 panels e and f). This occurs on two post-precipitation flights (RF02 and RF12) with the 2nd and 3rd coolest temperature profiles observed during TRANS^{2}Am (Figure S6). HNO_3-NO_3^- partitioning favors the aerosol phase under cool, high-HNO_3 conditions;

however, chamber experiments conducted under dry conditions (< 40% RH), where the particles may be solid or semi-solid, have shown that the time required to reach gas-aerosol equilibrium significantly increases from < 1 min for liquid particles to >> 10 min for solid/semi-solid particles due to kinetic mass transfer limitations imposed by low-viscosity particle-phase organics (Liggio et al., 2011). We find worsened model-observation agreement in E-AIM at RH <40% (Figure S7 and Figure S8), similar to a previous work that used ISORROPIA to study HNO_3-NO_3^- partitioning (Guo et al., 2016). These results suggest E-AIM might be correct in predicting NH_4NO_3 formation is favorable under the observed cool, dry, high-HNO_3 conditions, but its instantaneous equilibrium assumption may be unsuitable for application to observations made in concentrated AFO plumes or cool, dry conditions and result in the overprediction of NH_4^+ and NO_3^-.

3.3.1. Case Study 1: Cool and Humid Conditions (RF08)

Figure 5 shows a time series of observed as well as modeled aerosol species concentrations (panel a) and meteorological parameters (panel b) for RF08 on August 13, 2021 in the context of the entire campaign (panels c-e). Exceptionally cool conditions (relative to the rest of the campaign) on RF08 drive NH_4NO_3 formation, and the model is able to capture the temporal variability of the observed inorganic gas-aerosol partitioning on this flight. Panel (a) of Figure 5 shows the nanoequivalents (i.e., nmol m^{-3} × ion charge such that 1 nmol m^{-3} = 1 neq m^{-3} for NH_4^+ and NO_3^-, and 1 nmol m^{-3} = 2 neq m^{-3} for SO_4^{2-}) of modeled and observed cations and anions, and the model captures the temporal trends of both NH_4^+ and NO_3^-, replicating NH_4^+ and NO_3^- well (r = 0.52 for NH_4^+ and r = 0.88 for NO_3^-), with generally higher concentrations observed in the first half of the flight and lower concentrations in the second half. Compared to all other flights of Phase I of TRANS^{2}Am, this flight had exceptionally cool, humid conditions and this coincided with higher observed NO_3^-. Observed NO_3^- on RF08 is approximately 3 times higher than the

average over the entire campaign (Table S1) and accounts for 50% of observed NO_3^- greater than 1 µg m^{-3}. High TNO_3 is favorable for NH_4NO_3 formation; however, TNO_3 on RF08 is the lowest amongst all flights (Figure S5), so TNO_3 concentrations did not drive NH_4NO_3 on RF08. RH is consistently > 60% throughout RF08 (Figure 5 panel e); 60% is an approximate threshold above which spontaneous water uptake occurs and further favors the partitioning of NH_x and TNO_3 into the particle-phase (Wexler and Seinfeld, 1991). RF08 also has the coolest temperature conditions encountered during the campaign, with a surface temperature near 20˚C rather than ~30˚C for most other flights. The uncharacteristically cool, humid conditions may be partially explained by the flight time since RF08 was conducted in the morning (~9:00-11:30), as opposed to most other flights conducted in the early afternoon. There are no precipitation events on this day or the day before. Sensitivity tests show that NH_4NO_3 formation is much more sensitive to temperature (see Figure 7 and Section 3.4 for further discussion) than relative humidity (Figure S9). This implies cool temperatures drove NH_4NO_3 formation on RF08, and warm temperatures likely inhibited NH_4NO_3 formation on all other flights.

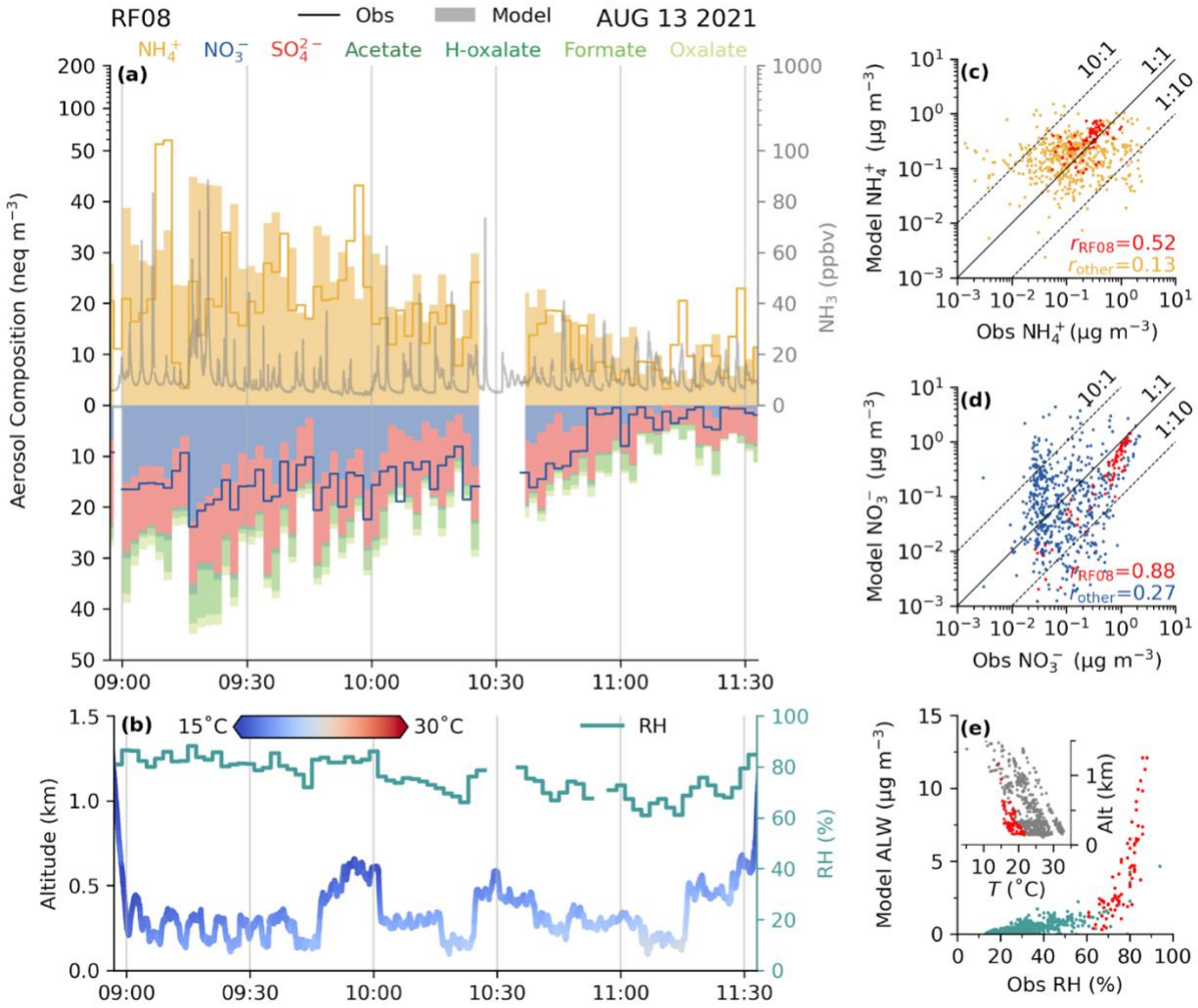

Figure 5. Time series of model and observations for RF08 (left) and model vs observations comparisons of RF08 and all other flights (right). (a): Aerosol composition in nanoequivalents per cubic meter (neq m^{-3}) on the left y-axis and gas phase measurements in ppbv on the right y-axis. At STP (273.15 K and 1 atm), 1 ppbv ≈ 45 nmol m^{-3} ≈ 2.8 μg m^{-3} for NH_3 ≈ 0.75 μg m^{-3} HNO_3. (b): Time series of altitude colored by temperature on the left y-axis and relative humidity on the right y-axis. (c): Modeled vs observed NH_4^+ and r-value for RF08 in red and all other flights in yellow. Lines represent 10:1, 1:1, and 1:10, as labeled. R-values for each (d): Same as (e), except for NO_3^- and other flights are blue. (e): Modeled aerosol liquid water (ALW) vs. observed relative humidity for RF08 in red vs all other flights in green. Inset axes show temperature profile for RF08 vs. all other flights. Note HNO_3 data is missing on RF08.

HNO_3 measurements for this flight did not pass quality control. Our model calculations conservatively assume that HNO_3 did not contribute to the TNO_3 input to the model because preliminary measurements of HNO_3 were very low (mean = -1.1 ppbv) and below the zero signal. As the model generally predicts the correct amount of NO_3^- during this flight, this corroborates our assumption that HNO_3 contributed trivially to TNO_3.

3.3.2. Case Study 2: Warm and Dry Conditions (RF02)

Figure 6 shows the same time series and scatter plots as in Figure 5 but for RF02 on August 4, 2021. RF02 is emblematic of many of the flights conducted on dry, warm conditions in the early afternoon during Phase I of TRANS^{2}Am, even though it occurred after a precipitation event and has the third coolest temperature profile (Figure S4). NH_4NO_3 formation appears to be generally inhibited by hot temperatures in summertime northeastern Colorado. Temperatures were warm (20 - 25 ˚C) close to the surface (< 200 m agl) throughout the afternoon, and RH was largely < 60%, where aerosol water uptake is limited to 2.5 µg m^{-3} or less. RF02 is one of 3 flights (also RF12 and RF13) where observed total nitrate is dominantly in the aerosol-phase in the first half of the flight and then dominantly in the gas-phase in the second half of the flight. Under these conditions, the model is able to capture the range of observed NH_4^+ and NO_3^-, but not the temporal variability ($r = 0.24$ and $r = -0.21$ for NH_4^+ and NO_3^-, respectively).

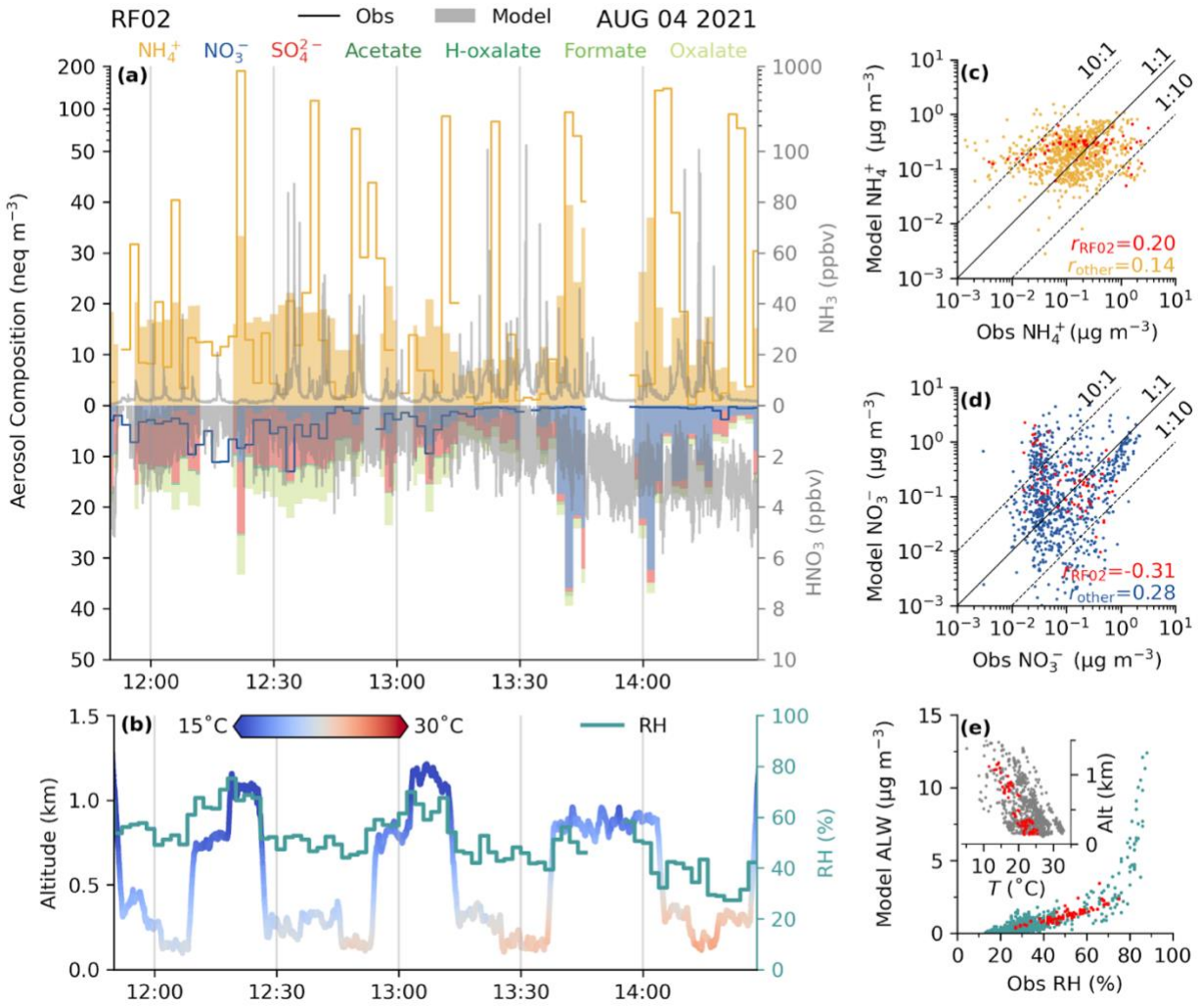

Figure 6. Same as Figure 5 except for RF02.

In Figure 6, NH_4^+ observations range from 10^{-3} to 10^{1} μg m^{-3}, but the model only predicts NH_4^+ between 10^{-1} to 10^{0} μg m^{-3}. This is possibly because the 2-minute resolution is too coarse to capture the sub-2-minute plume transect time and NH_3 variability. Model underestimates of NH_4^+ may also be attributable to unmeasured anions because the model assumes a neutral charge balance between cations and anions. Schlag et al. (2017) attributed excess NH_4^+ (NH_4^+ not associated with NO_3^- and SO_4^{2-}) to (di-)carboxylic acids, which can be enhanced by clouds and smoke. Stahl et al. (2021) found higher concentrations of total organic carbon in air masses influenced by biomass

burning during the CAMP^{2}Ex campaign. Data on 8 of the 10 flights used in this study were collected on smoke-impacted days, so we conduct sensitivity tests to examine the influence of smoke on the modeled NH_3-HNO_3-NH_4NO_3 partitioning (See Section 1 in SI for further discussion). In short, when the three most abundant (di-)carboxylic acids in the atmosphere (formate, oxalate, and acetate) are included in the mode input, the distributions of NH_4^+ and NO_3^- shift towards higher concentrations to better match observations (Figure S1 panels a and b). Further sensitivity tests with a proxy for unmeasured organics added to the model input does not show improved model-observation agreement in NH_4^+ and NO_3^- (Figure S1 panels c and d), indicating smoke is likely not a major contributor to the NH_4^+ underprediction in E-AIM.

Figure 6 also shows an example of non-equilibrium behavior driving the model overprediction NH_4^+ and NO_3^- when ascending to lower temperatures aloft in the second half of the flight (13:40-14:05) when HNO_3 increases above ~2 ppbv and RH remains <60%. As discussed previously in Section 3.3, this is likely a result of non-equilibrium behavior driven by slow kinetic mass transfer in dry solid/semi-solid aerosols. Although for scenarios like this, the model does not consistently capture the temporal variability of NH_3-NH_4^+ and HNO_3-NO_3^- partitioning, the model is able to consistently capture the range of NH_4^+ and NO_3^- in aggregate across the campaign (Figure 4).

3.4 Temperature-Sensitivity of Gas-Aerosol Partitioning during TRANS^{2}Am

Figure 7 shows the modeled effect of temperature and NH_x on gas-aerosol partitioning in and out of AFO plumes, and we find inorganic gas-aerosol partitioning is especially sensitive to temperature and NH_x during TRANS^{2}Am. In this simple water-SO_4^{2-}-NO_3^--NH_4^+ system with no organics or other inorganics, TNO_3, SO_4^{2-}, and RH are set to the average observed values during TRANS^{2}Am. The formation of NH_4NO_3 is inhibited by low NH_x and/or warm temperatures in the

light pink region and driven by high NHx and/or cool temperatures in the dark blue region. Between these two regimes, the formation of NH_4NO_3 is determined by a balance between temperature and NH_x. The range of observed NH_x and temperature is marked by the black outline, and observations are either characterized by regimes where NH_4NO_3 formation and partitioning to the aerosol phase is either (1) inhibited by warm temperatures and/or low NH_x (light pink region) or (2) very sensitive to both temperature and NH_x (steep NO_3/TNO_3 gradient in red, yellow, and green areas). The majority of observations fall in the first category, with 70% in the < 5% modeled NO_3^-/TNO_3 region and 92% in the modeled NO_3^-/TNO_3 < 20% region. In the HNO_3-limited regime of Figure 7 at $NH_x \geq 0.9$ μg m^{-3} (gas ratio > 1), NH_4NO_3 formation is still very sensitive to temperature and NH_3, indicating a transition regime between when NH_4NO_3 formation is solely sensitive to NH_3 and HNO_3. In this transition regime, at the same NH_x concentration, a temperature difference of 1˚C can result in a difference in NO_3^-/TNO_3 of as high as 12% (0.53 μg m^{-3} NH_4NO_3). Whereas Figure 7 shows model results from a simplified aerosol system, NH_3-HNO_3-NH_4NO_3 partitioning in the ambient atmosphere is affected by complex, non-linear relationships between temperature, RH (for aqueous aerosols), and concentrations of TNO_3, SO_4^{2-}, and other non-/semivolatile inorganic and organic compounds. We conduct sensitivity tests for various HNO_3 concentrations and RH observed during TRANS^{2}Am and find that the NH_4NO_3 mass concentration varies when TNO_3 increases, but the NO_3^- fraction of TNO_3 as a function of temperature and NH_x remains similar (Figure S10) and the majority observations still fall within the < 20% modeled NO_3^-/TNO_3 region (Table S2).

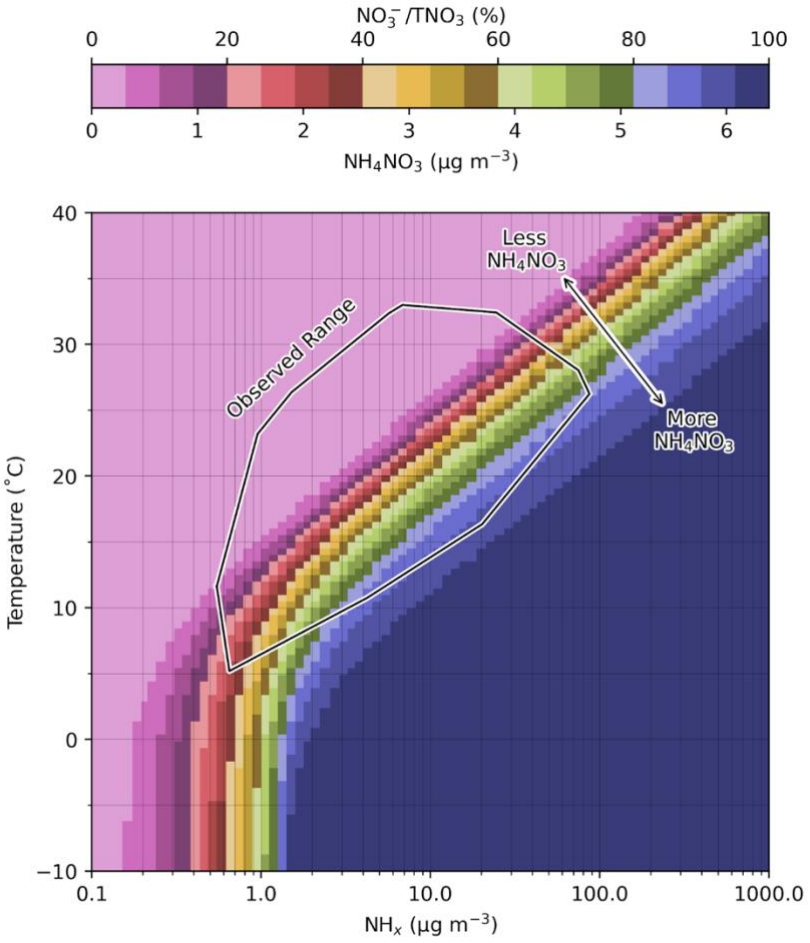

Figure 7. Modeled NH_4NO_3 and total nitrate partitioning (colorbar) for a sulfate-nitrate-ammonium system with fixed total nitrate, total sulfate, and RH for a range of temperatures and total ammonia concentrations. RH and TNO_3 are set to dry, median total nitrate conditions. The black outline shows the observed range of temperatures and NH_x during $TRANS^2Am$.

NH_4NO_3 formation can be sensitive to NH_3 in summertime AFO outflow even though it is largely HNO_3-limited. Figure S11 shows the change in modeled NH_4^+ and NO_3^- for simulations where NH_x and TNO_3 were respectively set to half of their measured concentrations. When NH_x is halved, modeled NH_4^+ and NO_3^- decrease in locations that are NH_3-limited. However, there are air masses sampled in the HNO_3-limited regime where NH_4^+ and NO_3^- also decrease. Similarly, when TNO_3 is halved, modeled NH_4^+ and NO_3^- consistently decrease in air masses in the HNO_3-limited regime; a decrease is also predicted for some NH_3-limited locations. This implies that many

air masses are sensitive to both NH_3 and HNO_3, and reducing NH_3 emissions may still be effective in reducing NH_4NO_3 concentrations.

Temperature appears to be a strong driver of inorganic gas-aerosol partitioning, so accurate measurements are critical. The gas-aerosol equilibrium of the NH_3-HNO_3-NH_4NO_3 aerosol system is very sensitive to temperature (e.g., Stelson et al., 1979). Temperature measurements could be complicated by measurement errors or the cabin temperature within the research aircraft being warmer than the surrounding atmosphere. We showed in Figure 7 that temperature differences as small as 1 ˚C can result in a difference in a modeled NH_4NO_3 as large as 12%, so small errors in the temperature measurement that is inputted into the model may also drive model-observation disagreement. We investigate whether a cabin-ambient temperature gradient may have driven aerosol evaporation in the PILS inlet line, leading to a low bias in aerosol measurements, especially when the plane ascends to cooler ambient temperatures between target facilities. Internal cabin temperature was not measured, so we are unable to investigate whether model-observation agreement of NH_4^+ and NO_3^- deteriorated when cabin temperature increased. Instead, we assume a dry NH_4NO_3 aerosol and calculate the change in the equilibrium product of $[NH_3][HNO_3]$ for a change in a range of atmospherically relevant temperatures based on kinetic mass transfer equations from Dahneke (1983) and NH_4NO_3 equilibrium constants based on Stelson and Seinfeld (1982) (Figure S12). Further details for this calculation can be found in Section 5 of the SI. We find that the transit time in the PILS inlet (2 seconds) is too short for significant evaporation (50% mass loss) to occur (Figure S13). Significant cabin-ambient gradients in equilibrium $[NH_3][HNO_3]$ (> 10 $ppbv^2$) occur when ambient temperatures are <30˚C and cabin temperatures are > 25˚C; however, it would take significantly longer than the transit time in the PILS inlet (≥10 seconds vs 2 seconds) for significant evaporation to occur. Significant mass loss only occurs at cabin and

ambient temperatures >30˚C, when the change in equilibrium $[NH_3][HNO_3]$ is small (<10 $ppbv^2$). Thus, a cabin-ambient temperature gradient may not be driving model-observation disagreement, but errors in temperature measurements may be a potential source of uncertainty in our thermodynamic modeling.

3.5 Modeling the Seasonality of NH_4NO_3 Formation

Figure 8 shows the distribution of NH_x, TNO_3, and SO_4^{2-} measured during Phase I of TRANS^{2}Am relative to the weekly measurements of NH_x, TNO_3, and SO_4^{2-} from mid-March to mid-October in 2014-2019 (excluding 2018) at the Weld County Tower surface monitoring site in Greeley, CO. Greeley is an urban (population = 110,000) area within the study region and immediately surrounded by a large number of AFOs (Figure 1). These long-term surface-based measurements indicate no strong seasonality in NH_x, TNO_3, and SO_4^{2-} concentrations in close proximity to AFOs and urban traffic emissions.

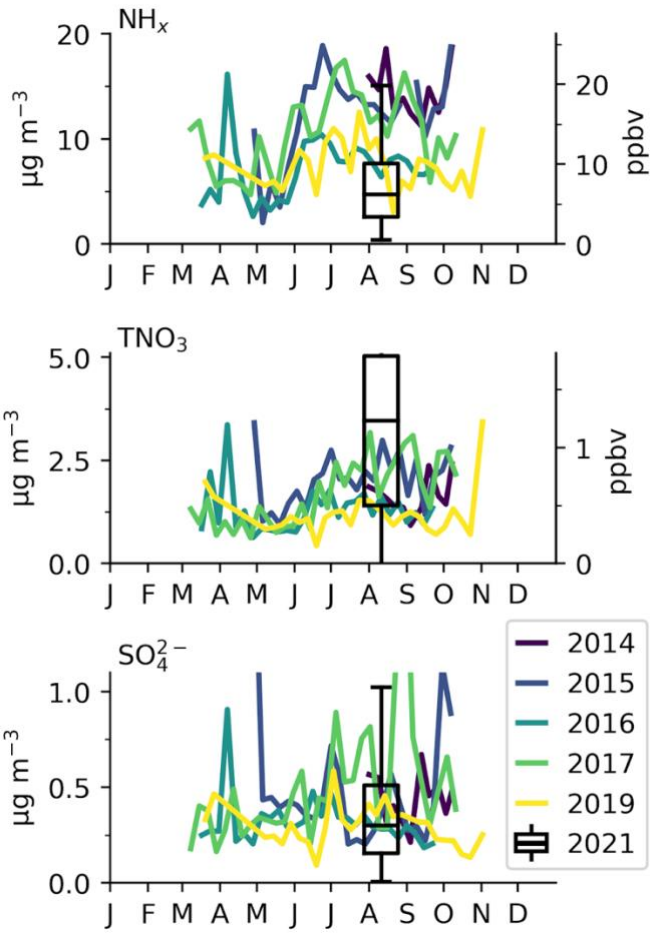

Figure 8. Weekly URG denuder/filter pack measurements of NH_x (top), TNO_3 (middle), and sulfate (bottom) in µg m^{-3} (left y-axis) and ppbv (right y-axis) at ambient temperature and pressure for March-October 2014-2017 and 2019 at the Weld County Tower surface monitoring site (40.386˚N, 104.737˚W) in Greeley, CO colored by year. Boxplot of TRANS^{2}Am Phase I measurements in 2021 are in black. Tails represent 1.5*IQR and extend from -0.9 µg m^{-3} to 8.7 µg m^{-3} for TNO_3.

2-minute averaged NH_x concentrations observed during TRANS^{2}Am are lower than long-term observations, and there are several potential reasons why we might expect this: (1) NH_x is dominated by NH_3, and NH_3 was measured aloft (300 - 1500 m agl) during TRANS^{2}Am. Away from individual facilities, NH_3 typically maximizes at 10 m agl (Li et al., 2014), and (2) the aircraft has sampled a much larger region and range of altitudes than represented by the ground observations.

TNO_3 measured during TRANS^{2}Am is higher than the URG measurements, which may be because (1) the diurnal cycle of HNO_3 and (2) the influence from wildfire smoke. During summertime, active photochemistry drives a peak in HNO_3 between 11AM - 2 PM local time Lindaas et al. (2017). Thus, most of the TRANS^{2}Am flights were conducted when HNO_3 concentrations are largest. Summer 2021 was also an active wildfire season, and HNO_3 is the second highest constituent of NO_y in aged wildfire smoke at low altitudes (Juncosa Calahorrano et al., 2020).

Lastly, sulfate concentrations are consistent between TRANS^{2}Am and the long–term measurements at Weld County Tower, and do not exhibit a strong seasonality. This is consistent with Chan et al. (2018), who observed no sulfate seasonality across the US after 2008. Since neither NH_x, TNO_3, nor SO_4^{2-} show a strong seasonal pattern, we model the seasonality of NH_4NO_3 formation by varying only temperature.

We investigate the seasonality of NH_4NO_3 formation for average temperature conditions in northeastern Colorado using E-AIM and hypothesize the existence of significantly higher concentrations in spring/autumn and winter due to the strong sensitivity to temperature. We model spring/autumn by lowering the model temperature by 10˚C relative to campaign observations during the summer, and winter conditions by lowering the temperature by 20˚C to capture the seasonal temperature ranges in this study region.

Figure 9 shows consistently more NH_4^+ and NO_3^- during these cooler seasons, indicating NH_4NO_3 formation is thermodynamically favorable significantly more often in spring/autumn and winter. Instances of significant NH_4NO_3 formation > 1, > 3, and > 5 µg m^{-3} are summarized in Table 2, and NH_4NO_3 > 1 µg m^{-3} is almost 10 times more likely in the winter than in the summer. In August 2021, no NH_4NO_3 > 3 µg m^{-3} was observed and very little was modeled, but the model

suggests that significantly more is likely present in spring/autumn and winter. These modeling results imply that even though NH_4NO_3 formation is HNO_3-limited and generally inhibited by hot temperatures during TRANS^{2}Am, high concentrations of NH_3 (> 5 ppbv) could contribute to significant $PM_{2.5}$ formation under cooler conditions given the weak seasonal cycle in precursors (Figure 8).

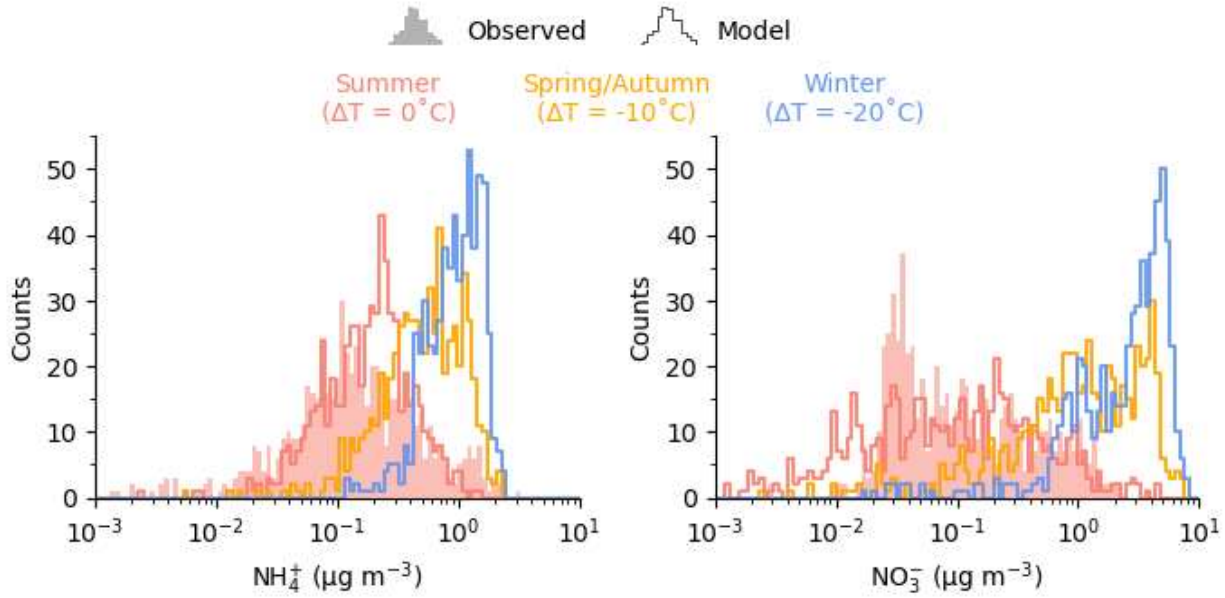

Figure 9. Histograms of observed and modeled NH_4^+ (left) and NO_3^- (right). Red shade is observations during summer, red line is model with observed temperature during summer (ΔT = 0 ˚C), yellow line is model with observed temperature minus 10˚C (ΔT = -10˚C) to simulate spring/fall, and blue line is model with observed temperature minus 20˚C (ΔT = -20˚C) to simulate winter.

Table 2. Percent of observed and modeled NH_4NO_3 greater than mass concentrations by season.

	Observed	Modeled		
	Summer	Summer ($\Delta T = 0^{\circ}C$)	Spring/Autumn ($\Delta T = -10^{\circ}C$)	Winter ($\Delta T = -20^{\circ}C$)
$NH_4NO_3 \geq 1$ μg m^{-3}	10% (61/634)	9% (56/612)	61% (375/612)	88% (537/612)
$NH_4NO_3 \geq 3$ μg m^{-3}	0% (0/634)	2% (10/612)	28% (171/612)	60% (365/612)
$NH_4NO_3 \geq 5$ μg m^{-3}	0% (0/634)	0.3% (2/612)	11% (69/612)	35% (213/612)

We evaluated whether we expect NH_3 plumes from AFOs to enhance NH_4NO_3 concentrations relative to background during cooler seasons (Figure S14). Summertime and wintertime NH_4NO_3 formation in and out of plumes is more sensitive to the temperature differences between seasons than the differences in NH_3 in and out of a plume, whereas NH_4NO_3 formation in spring/autumn is sensitive to both temperature and the NH_3 changes (Figure S14). In the summer, both the model and observations agree NH_4NO_3 is typically < 1 μg m^{-3} both in the background (NH_3 < 20 ppbv) and in plumes ($NH_3 \geq 20$ ppbv) and inhibited by warm temperatures. In the winter, the median NH_4NO_3 increases from 2.8 μg m^{-3} in the background to 4.6 μg m^{-3} in plumes. In spring/autumn, the median NH_4NO_3 is still relatively low (0.9 μg m^{-3}) in the background but increases to 3.6 μg m^{-3} in plumes. These results suggest a transition from summertime temperature-inhibited NH_4NO_3 formation to wintertime temperature-saturated NH_4NO_3 formation and an intermediate temperature- and NH_3-sensitive regime in the transitional seasons.

4 CONCLUSIONS

In this work, we present a unique application of the E-AIM aerosol thermodynamic to agricultural plumes from animal feeding operations under hot, dry summertime conditions in Northern Colorado. With a holistic dataset of aircraft-based gas-phase and aerosol-phase measurements from Phase I of the TRANS^{2}Am campaign, we (1) study the sensitivity of NH_4NO_3 formation to AFO emissions of NH_3, and (2) explore the seasonality of NH_4NO_3 formation in northeastern Colorado. We find that:

1. Summertime northeastern Colorado is NH_3-rich and HNO_3-limited.
2. During August 2021, the observed range of NH_3-NH_4^+ and HNO_3-NO_3^- partitioning on aggregate can generally be explained by the E-AIM aerosol thermodynamic model with NH_x ($NH_3 + NH_4^+$), TNO_3 ($HNO_3 + NO_3^-$), SO_4^{2-}, oxalate, formate, acetate as inputs.
3. The observed NH_4NO_3 concentration is usually <1 μg m^{-3} above 300 m agl and its formation is thermodynamically inhibited by hot temperatures.
4. The NH_4NO_3 formation observed during Phase I of TRANS^{2}Am is especially sensitive to temperature and NH_x at conditions. The campaign sampled a wide range of NH_3 concentrations (0.5 - 114 ppbv, 2-min averages) and temperatures between 5 and 33℃. A small change in temperature of 1˚C under these ammonia concentrations can change NH_4NO_3 formation by as much as 12%.
5. We predict that NH_4NO_3 could reach substantial (> 1 μg m^{-3}) concentrations in northeastern Colorado due to cooler temperatures in spring/autumn and winter.

We demonstrate that with a comprehensive dataset of high temporal resolution aircraft-based gas-phase and aerosol-phase measurements, aerosol thermodynamic models can be

leveraged to study the inorganic gas-aerosol partitioning of the NH_3-HNO_3-NH_4NO_3 system from large NH_3 point sources. Thus, similar payloads that measure both NH_3 and HNO_3 gases and aerosols at high sub-hour resolutions can then also be used to study NH_3-NH_4^+ partitioning in agricultural regions. Future work should include similar measurements made under a wider range of conditions, particularly under cooler conditions.

4.1 Limitations and Future Work

The analysis presented here is limited to generally smoky, hot, dry summer afternoons in northeastern Colorado in August 2021 between 150-1500 m agl. Under these conditions, we find that NH_3-NH_4^+ is generally negligible within ~100 km of emission from AFOs due to thermodynamic inhibition by hot temperatures. However, modeling results suggest significant NH_3-NH_4^+ partitioning could occur under cooler temperatures. To draw more robust conclusions about NH_3-NH_4^+ outside of these conditions, there are several possible directions for future work.

Exploring the seasonality of NH_4NO_3 formation in northeastern Colorado in this analysis is limited by a lack of direct measurements. In our study, we have used multi-year observations from a surface monitoring station within the study region to assume we can predict NH_4NO_3 formation in spring/autumn and winter by changing only temperature in our model inputs. There are several possible approaches to sample at cooler temperatures, each with their own additional benefits:

1. Sampling during spring/autumn and winter in the same manner of TRANS^{2}Am would provide more direct observational constraints on model inputs of temperature, RH, and gas-phase and aerosol-phase concentrations used in our NH_4NO_3 seasonality analysis. Originally, springtime sampling was proposed for the TRANS^{2}Am campaign but was not conducted due to logistical reasons. Springtime sampling has the added advantages of (1)

possibly sampling spring thaw when nitrogen is released from waste piles/ponds and agricultural soil, which has been understudied (Kim et al. 2012), (2) additional agricultural NH_3 emissions from fertilizer application, and (3) increased frequency of upslope events to study nitrogen deposition in Rocky Mountain National Park.

2. Sampling throughout diurnal temperature cycles in summer in northeastern Colorado can capture temperature changes typically ranging from 15 ˚C in the early morning to 30 °C in the early afternoon and provide insight into the diurnal variation of NH_4NO_3 formation in NH_3-rich environments.
3. Sampling during and after summertime precipitation events are another opportunity to sample at cooler temperatures. Summertime temperatures in northeastern Colorado can be 5-10 °C lower during and the day after a precipitation event compared to no-precipitation days. Airborne sampling directly in precipitation would not be possible for the gas-phase instruments used during TRANS^{2}AM, but higher concentrations of NH_4NO_3 might be observed in the cooler, humid conditions afterwards. With additional planning, sampling in cold pools (i.e., localized cooler air masses due to convective evaporative cooling of rain) may also provide further insight into NH_4NO_3 formation from precipitation events. NH_3 emissions and NH_4^+ have been reported to decrease following precipitation on a weekly timescale (Aneja et al., 2003), but have not yet been studied at fine 2-minute temporal resolution.

Other limitations and directions for future work might include:

1. Sampling under a wider variety of conditions.

   We had expected increased NH_4NO_3 as agricultural high-NH_3 outflow mixes with urban high-HNO_3 air masses, but did not observe this in our data. Targeting periods when outflow

from the Denver metropolitan area (population = 3,000,000) moves northward into our study region may provide additional insight on NH_4NO_3 formation in urban-agricultural regions. Characterization of interannual variability may also provide interesting insights as summer 2023 in northeastern Colorado was anomalously cool and wet (Colorado Climate Center).

2. Incorporating 3-D chemical transport modeling to assess air quality controls.

   Models can provide insights into air quality responses to pollution controls that observations alone cannot. Models can be used to leverage a compilation of known atmospheric processes to understand complex non-linear responses to emissions. For example, Womak et al. (2019) used a zero-dimensional box model to show that HNO_3-limited wintertime NH_4NO_3 pollution in Salt Lake City is counter-intuitively responsive to VOC controls and not initially responsive to NOx controls. A regional air quality model (e.g., CMAQ, CAMx, WRF-Chem, high performance GEOS-Chem (GCHP) in conjunction with TRANS^{2}Am observations could assess the subgrid variability of NH_3-HNO_3-NH_4NO_3 partitioning and help improve the model representation of the contribution of NH_4NO_3 to $PM_{2.5}$.

3. Size-resolved Gas-Aerosol Modeling

   We implicitly assume an internally mixed aerosol population (i.e., all aerosols sampled have the same chemical composition), but this assumption may not hold, especially when also considering NH_3-HNO_3-NH_4NO_3 partitioning onto coarse mode (D_p > 3 µm) aerosols, which were not measured during TRANS^{2}Am. Previous studies have conducted size-resolved modeling of pH (e.g., Patoulias et al., 2021), in which the gas-aerosol partitioning is modeled individually for each size bin. This would require additional instrumentation

such an additional PILS instrument to measure PM_{10} aerosol composition to measure the size-resolved chemical composition of aerosols in the fine mode and coarse mode, but would not be possible without a larger aircraft given the limited power and space on the research aircraft used here.

BIBLIOGRAPHY

Aneja, V. P., Nelson, D. R., Roelle, P. A., Walker, J. T., & Battye, W. (2003). Agricultural ammonia emissions and ammonium concentrations associated with aerosols and precipitation in the southeast United States. *Journal of Geophysical Research: Atmospheres*, *108*(D4). https://doi.org/10.1029/2002JD002271

Ansari, A. S., & Pandis, S. N. (1998). Response of Inorganic PM to Precursor Concentrations. *Environmental Science & Technology*, *32*(18), 2706–2714. https://doi.org/10.1021/es971130j

Ayers, G. P., Gillett, R. W., & Gras, J. L. (1980). On the vapor pressure of sulfuric acid. *Geophysical Research Letters*, *7*(6), 433–436. https://doi.org/10.1029/GL007i006p00433

Bassett, M., & Seinfeld, J. H. (1983). Atmospheric equilibrium model of sulfate and nitrate aerosols. *Atmospheric Environment (1967)*, *17*(11), 2237–2252. https://doi.org/10.1016/0004-6981(83)90221-4

Behera, S. N., Sharma, M., Aneja, V. P., & Balasubramanian, R. (2013). Ammonia in the atmosphere: a review on emission sources, atmospheric chemistry and deposition on terrestrial bodies. *Environmental Science and Pollution Research*, *20*(11), 8092–8131. https://doi.org/10.1007/s11356-013-2051-9

Benedict, K. B., Chen, X., Sullivan, A. P., Li, Y., Day, D., Prenni, A. J., et al. (2013). Atmospheric concentrations and deposition of reactive nitrogen in Grand Teton National Park. *Journal of Geophysical Research: Atmospheres*, *118*(20), 11,875-11,887. https://doi.org/10.1002/2013JD020394

Benedict, K. B., Day, D., Schwandner, F. M., Kreidenweis, S. M., Schichtel, B., Malm, W. C., & Collett, J. L. (2013). Observations of atmospheric reactive nitrogen species in Rocky Mountain National Park and across northern Colorado. *Atmospheric Environment*, *64*, 66–76. https://doi.org/10.1016/j.atmosenv.2012.08.066

Benedict, K. B., Prenni, A. J., Sullivan, A. P., Evanoski-Cole, A. R., Fischer, E. V., Callahan, S., et al. (2018). Impact of Front Range sources on reactive nitrogen concentrations and deposition in Rocky Mountain National Park. *PeerJ*, *6*, e4759. https://doi.org/10.7717/peerj.4759

Chan, E. A. W., Gantt, B., & McDow, S. (2018). The reduction of summer sulfate and switch from summertime to wintertime PM2.5 concentration maxima in the United States. *Atmospheric Environment*, *175*, 25–32. https://doi.org/10.1016/j.atmosenv.2017.11.055

Chen, D., Yao, X., Chan, C. K., Tian, X., Chu, Y., Clegg, S. L., et al. (2022). Competitive Uptake of Dimethylamine and Trimethylamine against Ammonia on Acidic Particles in Marine Atmospheres. *Environmental Science & Technology*, *56*(9), 5430–5439. https://doi.org/10.1021/acs.est.1c08713

Cheng, B., Wang-Li, L., Meskhidze, N., Classen, J., & Bloomfield, P. (2021). Partitioning of NH3-NH4+ in the Southeastern U.S. *Atmosphere*, *12*(12), 1681. https://doi.org/10.3390/atmos12121681

Clegg, S. L., Brimblecombe, P., & Wexler, A. S. (1998). Thermodynamic Model of the System H+−NH4+−SO42-−NO3-−H2O at Tropospheric Temperatures. *The Journal of Physical Chemistry A*, *102*(12), 2137–2154. https://doi.org/10.1021/jp973042r

Colorado Climate Center. (2023). *August 2023 Colorado Monthly Climate Summary*. Retrieved from https://climate.colostate.edu/reports/2023Aug_climate_summary.pdf

Dahneke, B. (1983). Simple Kinetic Theory of Brownian Diffusion in Vapors and Aerosols. In R. E. Meyer (Ed.), *Theory of Dispersed Multiphase Flow* (pp. 97–133). Academic Press. https://doi.org/10.1016/B978-0-12-493120-6.50011-8

Day, D. E., Chen, X., Gebhart, K. A., Carrico, C. M., Schwandner, F. M., Benedict, K. B., et al. (2012). Spatial and temporal variability of ammonia and other inorganic aerosol species. *Atmospheric Environment*, *61*, 490–498. https://doi.org/10.1016/j.atmosenv.2012.06.045

Eilerman, S. J., Peischl, J., Neuman, J. A., Ryerson, T. B., Aikin, K. C., Holloway, M. W., et al. (2016a). Characterization of Ammonia, Methane, and Nitrous Oxide Emissions from Concentrated Animal Feeding Operations in Northeastern Colorado. *Environmental Science & Technology*, *50*(20), 10885–10893. https://doi.org/10.1021/acs.est.6b02851

Eilerman, S. J., Peischl, J., Neuman, J. A., Ryerson, T. B., Aikin, K. C., Holloway, M. W., et al. (2016b). Characterization of Ammonia, Methane, and Nitrous Oxide Emissions from Concentrated Animal Feeding Operations in Northeastern Colorado. *Environmental Science & Technology*, *50*(20), 10885–10893. https://doi.org/10.1021/acs.est.6b02851

Ellis, R. A., Murphy, J. G., Pattey, E., van Haarlem, R., O'Brien, J. M., & Herndon, S. C. (2010a). Characterizing a Quantum Cascade Tunable Infrared Laser Differential Absorption Spectrometer (QC-TILDAS) for measurements of atmospheric ammonia. *Atmospheric Measurement Techniques*, *3*(2), 397–406. https://doi.org/10.5194/amt-3-397-2010

Ellis, R. A., Murphy, J. G., Pattey, E., van Haarlem, R., O'Brien, J. M., & Herndon, S. C. (2010b). Characterizing a Quantum Cascade Tunable Infrared Laser Differential Absorption Spectrometer (QC-TILDAS) for measurements of atmospheric ammonia. *Atmospheric Measurement Techniques*, *3*(2), 397–406. https://doi.org/10.5194/amt-3-397-2010

Erisman, J. W., Sutton, M. A., Galloway, J., Klimont, Z., & Winiwarter, W. (2008). How a century of ammonia synthesis changed the world. *Nature Geoscience*, *1*(10), 636–639. https://doi.org/10.1038/ngeo325

Fang, Z., Dong, S., Huang, C., Jia, S., Wang, F., Liu, H., et al. (2023). On using an aerosol thermodynamic model to calculate aerosol acidity of coarse particles. *Journal of Environmental Sciences*. https://doi.org/10.1016/j.jes.2023.07.001

Fountoukis, C., & Nenes, A. (2007). ISORROPIA II: a computationally efficient thermodynamic equilibrium model for K^+–Ca^{2+}–Mg^{2+}–NH_4^+–Na^+–SO_4^{2-}–NO_3^-–Cl^-–H_2O aerosols. *Atmospheric Chemistry and Physics*, *7*(17), 4639–4659. https://doi.org/10.5194/acp-7-4639-2007

Friese, E., & Ebel, A. (2010). Temperature Dependent Thermodynamic Model of the System H^+–NH_4^+–Na^+–SO_4^{2-}–NO_3^-–Cl^-–H_2O. *The Journal of Physical Chemistry A*, *114*(43), 11595–11631. https://doi.org/10.1021/jp101041j

Galloway, J. N., Dentener, F. J., Capone, D. G., Boyer, E. W., Howarth, R. W., Seitzinger, S. P., et al. (2004). Nitrogen Cycles: Past, Present, and Future. *Biogeochemistry*, *70*(2), 153–226. https://doi.org/10.1007/s10533-004-0370-0

Guo, H., Sullivan, A. P., Campuzano-Jost, P., Schroder, J. C., Lopez-Hilfiker, F. D., Dibb, J. E., et al. (2016). Fine particle pH and the partitioning of nitric acid during winter in the northeastern United States. *Journal of Geophysical Research: Atmospheres*, *121*(17), 10,355-10,376. https://doi.org/10.1002/2016JD025311

Guo, H., Otjes, R., Schlag, P., Kiendler-Scharr, A., Nenes, A., & Weber, R. J. (2018). Effectiveness of ammonia reduction on control of fine particle nitrate. *Atmospheric Chemistry and Physics*, *18*(16), 12241–12256. https://doi.org/10.5194/acp-18-12241-2018

Hacker, J. M., Chen, D., Bai, M., Ewenz, C., Junkermann, W., Lieff, W., et al. (2016). Using airborne technology to quantify and apportion emissions of CH_4 and NH_3 from feedlots. *Animal Production Science*, *56*(3), 190–203. https://doi.org/10.1071/AN15513

Hand, J. L., Prenni, A. J., Copeland, S., Schichtel, B. A., & Malm, W. C. (2020). Thirty years of the Clean Air Act Amendments: Impacts on haze in remote regions of the United States (1990–2018). *Atmospheric Environment*, *243*, 117865. https://doi.org/10.1016/j.atmosenv.2020.117865

Hennigan, C. J., Izumi, J., Sullivan, A. P., Weber, R. J., & Nenes, A. (2015). A critical evaluation of proxy methods used to estimate the acidity of atmospheric particles. *Atmospheric Chemistry and Physics*, *15*(5), 2775–2790. https://doi.org/10.5194/acp-15-2775-2015

Hristov, A. N., Hanigan, M., Cole, A., Todd, R., McAllister, T. A., Ndegwa, P. M., & Rotz, A. (2011). Review: Ammonia emissions from dairy farms and beef feedlots. *Canadian Journal of Animal Science*, *91*(1), 1–35. https://doi.org/10.4141/CJAS10034

Jimenez, J. L., Canagaratna, M. R., Donahue, N. M., Prevot, A. S. H., Zhang, Q., Kroll, J. H., et al. (2009). Evolution of Organic Aerosols in the Atmosphere. *Science*, *326*(5959), 1525–1529. https://doi.org/10.1126/science.1180353

Juncosa Calahorrano, J., Pollack, I. B., Sullivan, A. P., Roscioli, J. R., Caulton, D. R., McCabe, M. E., et al. (in press). Summertime airborne measurements of ammonia emissions from cattle feedlots and dairies in northeastern Colorado. *Journal of Geophysical Research: Atmospheres*.

Juncosa Calahorrano, J. F., Lindaas, J., O'Dell, K., Palm, B. B., Peng, Q., Flocke, F., et al. (2021). Daytime Oxidized Reactive Nitrogen Partitioning in Western U.S. Wildfire Smoke Plumes. *Journal of Geophysical Research: Atmospheres*, *126*(4), e2020JD033484. https://doi.org/10.1029/2020JD033484

Kakavas, S., Patoulias, D., Zakoura, M., Nenes, A., & Pandis, S. N. (2021). Size-resolved aerosol pH over Europe during summer. *Atmospheric Chemistry and Physics*, *21*(2), 799–811. https://doi.org/10.5194/acp-21-799-2021

Kim, D.-G., Vargas, R., Bond-Lamberty, B., & Turetsky, M. R. (2012). Effects of soil rewetting and thawing on soil gas fluxes: a review of current literature and suggestions for future research. *Biogeosciences*, *9*(7), 2459–2483. https://doi.org/10.5194/bg-9-2459-2012

Kim, Y. P., Seinfeld, J. H., & Saxena, P. (1993). Atmospheric Gas-Aerosol Equilibrium I. Thermodynamic Model. *Aerosol Science and Technology*, *19*(2), 157–181. https://doi.org/10.1080/02786829308959628

Kulmala, M., & Laaksonen, A. (1990). Binary nucleation of water–sulfuric acid system: Comparison of classical theories with different H2SO4 saturation vapor pressures. *The Journal of Chemical Physics*, *93*(1), 696–701. https://doi.org/10.1063/1.459519

Li, Y., Thompson, T. M., Van Damme, M., Chen, X., Benedict, K. B., Shao, Y., et al. (2017a). Temporal and spatial variability of ammonia in urban and agricultural regions of northern Colorado, United States. *Atmospheric Chemistry and Physics*, *17*(10), 6197–6213. https://doi.org/10.5194/acp-17-6197-2017

Li, Y., Thompson, T. M., Van Damme, M., Chen, X., Benedict, K. B., Shao, Y., et al. (2017b). Temporal and spatial variability of ammonia in urban and agricultural regions of northern Colorado, United States. *Atmospheric Chemistry and Physics*, *17*(10), 6197–6213. https://doi.org/10.5194/acp-17-6197-2017

Liggio, J., Li, S.-M., Vlasenko, A., Stroud, C., & Makar, P. (2011). Depression of Ammonia Uptake to Sulfuric Acid Aerosols by Competing Uptake of Ambient Organic Gases. *Environmental Science & Technology*, *45*(7), 2790–2796. https://doi.org/10.1021/es103801g

Lindaas, J., Farmer, D. K., Pollack, I. B., Abeleira, A., Flocke, F., Roscioli, R., et al. (2017). Changes in ozone and precursors during two aged wildfire smoke events in the Colorado Front Range in summer 2015. *Atmospheric Chemistry and Physics*, *17*(17), 10691–10707. https://doi.org/10.5194/acp-17-10691-2017

Liu, L., Xu, W., Lu, X., Zhong, B., Guo, Y., Lu, X., et al. (2022). Exploring global changes in agricultural ammonia emissions and their contribution to nitrogen deposition since 1980. *Proceedings of the National Academy of Sciences*, *119*(14), e2121998119. https://doi.org/10.1073/pnas.2121998119

Luo, Z., Zhang, Y., Chen, W., Van Damme, M., Coheur, P.-F., & Clarisse, L. (2022). Estimating global ammonia (NH_3) emissions based on IASI observations from 2008 to 2018. *Atmospheric Chemistry and Physics*, *22*(15), 10375–10388. https://doi.org/10.5194/acp-22-10375-2022

Marple, V. A., Rubow, K. L., & Behm, S. M. (1991). A Microorifice Uniform Deposit Impactor (MOUDI): Description, Calibration, and Use. *Aerosol Science and Technology*, *14*(4), 434–446. https://doi.org/10.1080/02786829108959504

McCabe, M. E., Pollack, I. B., Fischer, E. V., Steinmann, K. M., & Caulton, D. R. (2023). Technical note: Isolating methane emissions from animal feeding operations in an interfering location. *Atmospheric Chemistry and Physics*, *23*(13), 7479–7494. https://doi.org/10.5194/acp-23-7479-2023

McManus, J. B., Kebabian, P. L., & Zahniser, M. S. (1995). Astigmatic mirror multipass absorption cells for long-path-length spectroscopy. *Applied Optics*, *34*(18), 3336–3348. https://doi.org/10.1364/AO.34.003336

McManus, J. Barry, Zahniser, M. S., Jr, D. D. N., Shorter, J. H., Herndon, S. C., Wood, E. C., & Wehr, R. (2010). Application of quantum cascade lasers to high-precision atmospheric trace gas measurements. *Optical Engineering*, *49*(11), 111124. https://doi.org/10.1117/1.3498782

Metzger, S., Mihalopoulos, N., & Lelieveld, J. (2006). Importance of mineral cations and organics in gas-aerosol partitioning of reactive nitrogen compounds: case study based on MINOS results. *Atmospheric Chemistry and Physics*, *6*(9), 2549–2567. https://doi.org/10.5194/acp-6-2549-2006

Miller, D. J., Sun, K., Tao, L., Pan, D., Zondlo, M. A., Nowak, J. B., et al. (2015). Ammonia and methane dairy emission plumes in the San Joaquin Valley of California from individual feedlot to regional scales. *Journal of Geophysical Research: Atmospheres*, *120*(18), 9718–9738. https://doi.org/10.1002/2015JD023241

Murphy, J. G., Gregoire, P. K., Tevlin, A. G., Wentworth, G. R., Ellis, R. A., Markovic, M. Z., & VandenBoer, T. C. (2017). Observational constraints on particle acidity using measurements and modelling of particles and gases. *Faraday Discussions*, *200*(0), 379–395. https://doi.org/10.1039/C7FD00086C

Nah, T., Guo, H., Sullivan, A. P., Chen, Y., Tanner, D. J., Nenes, A., et al. (2018). Characterization of aerosol composition, aerosol acidity, and organic acid partitioning at an agriculturally intensive rural southeastern US site. *Atmospheric Chemistry and Physics*, *18*(15), 11471–11491. https://doi.org/10.5194/acp-18-11471-2018

Nair, A. A., & Yu, F. (2020). Quantification of Atmospheric Ammonia Concentrations: A Review of Its Measurement and Modeling. *Atmosphere*, *11*(10), 1092. https://doi.org/10.3390/atmos11101092

NEI (National Emissions Inventory). (2020). United States Environmental Protection Agency. Retrieved August 15, 2023, from https://www.epa.gov/air-emissions-inventories/2020-national-emissions-inventory-nei-data

Neuman, J. A., Ryerson, T. B., Huey, L. G., Jakoubek, R., Nowak, J. B., Simons, C., & Fehsenfeld, F. C. (2003). Calibration and Evaluation of Nitric Acid and Ammonia Permeation Tubes by UV Optical Absorption. *Environmental Science & Technology*, *37*(13), 2975–2981. https://doi.org/10.1021/es0264221

Orsini, D. A., Ma, Y., Sullivan, A., Sierau, B., Baumann, K., & Weber, R. J. (2003). Refinements to the particle-into-liquid sampler (PILS) for ground and airborne measurements of water soluble aerosol composition. *Atmospheric Environment*, *37*(9), 1243–1259. https://doi.org/10.1016/S1352-2310(02)01015-4

Pan, D., Benedict, K. B., Golston, L. M., Wang, R., Collett, J. L., Tao, L., et al. (2021). Ammonia Dry Deposition in an Alpine Ecosystem Traced to Agricultural Emission Hotpots. *Environmental Science & Technology*, *55*(12), 7776–7785. https://doi.org/10.1021/acs.est.0c05749

Petters, M. D., & Kreidenweis, S. M. (2007). A single parameter representation of hygroscopic growth and cloud condensation nucleus activity. *Atmospheric Chemistry and Physics*, *7*(8), 1961–1971. https://doi.org/10.5194/acp-7-1961-2007

Pollack, I. B., Lindaas, J., Roscioli, J. R., Agnese, M., Permar, W., Hu, L., & Fischer, E. V. (2019). Evaluation of ambient ammonia measurements from a research aircraft using a closed-path QC-TILDAS operated with active continuous passivation. *Atmospheric Measurement Techniques*, *12*(7), 3717–3742. https://doi.org/10.5194/amt-12-3717-2019

Pollack, I. B., McCabe, M. E., Caulton, D. R., & Fischer, E. V. (2022). Enhancements in Ammonia and Methane from Agricultural Sources in the Northeastern Colorado Front Range Using Observations from a Small Research Aircraft. *Environmental Science & Technology*. https://doi.org/10.1021/acs.est.1c07382

Pope, C. A., Ezzati, M., & Dockery, D. W. (2009). Fine-Particulate Air Pollution and Life Expectancy in the United States. *New England Journal of Medicine*, *360*(4), 376–386. https://doi.org/10.1056/NEJMsa0805646

Pun, B. K., Griffin, R. J., Seigneur, C., & Seinfeld, J. H. (2002). Secondary organic aerosol 2. Thermodynamic model for gas/particle partitioning of molecular constituents. *Journal of Geophysical Research: Atmospheres*, *107*(D17), AAC 4-1-AAC 4-15. https://doi.org/10.1029/2001JD000542

Pye, H. O. T., Nenes, A., Alexander, B., Ault, A. P., Barth, M. C., Clegg, S. L., et al. (2020). The acidity of atmospheric particles and clouds. *Atmospheric Chemistry and Physics*, *20*(8), 4809–4888. https://doi.org/10.5194/acp-20-4809-2020

Robarge, W. P., Walker, J. T., McCulloch, R. B., & Murray, G. (2002). Atmospheric concentrations of ammonia and ammonium at an agricultural site in the southeast United States. *Atmospheric Environment*, *36*(10), 1661–1674. https://doi.org/10.1016/S1352-2310(02)00171-1

Roedel, W. (1979). Measurement of sulfuric acid saturation vapor pressure; Implications for aerosol formation by heteromolecular nucleation. *Journal of Aerosol Science*, *10*(4), 375–386. https://doi.org/10.1016/0021-8502(79)90032-6

Rood, M. J., Shaw, M. A., Larson, T. V., & Covert, D. S. (1989). Ubiquitous nature of ambient metastable aerosol. *Nature*, *337*(6207), 537–539. https://doi.org/10.1038/337537a0

Roscioli, J. R., Zahniser, M. S., Nelson, D. D., Herndon, S. C., & Kolb, C. E. (2016). New Approaches to Measuring Sticky Molecules: Improvement of Instrumental Response Times Using Active Passivation. *The Journal of Physical Chemistry A*, *120*(9), 1347–1357. https://doi.org/10.1021/acs.jpca.5b04395

Russell, A. G., McRae, G. J., & Cass, G. R. (1983). Mathematical modeling of the formation and transport of ammonium nitrate aerosol. *Atmospheric Environment (1967)*, *17*(5), 949–964. https://doi.org/10.1016/0004-6981(83)90247-0

Schlag, P., Rubach, F., Mentel, T. F., Reimer, D., Canonaco, F., Henzing, J. S., et al. (2017). Ambient and laboratory observations of organic ammonium salts in PM1. *Faraday Discussions*, *200*(0), 331–351. https://doi.org/10.1039/C7FD00027H

Schobesberger, S., D'Ambro, E. L., Vettikkat, L., Lee, B. H., Peng, Q., Bell, D. M., et al. (2023). Airborne flux measurements of ammonia over the southern Great Plains using chemical ionization mass spectrometry. *Atmospheric Measurement Techniques*, *16*(2), 247–271. https://doi.org/10.5194/amt-16-247-2023

Snider, J., Petters, M., Takagi, H., Liu, P., Lukens, D., Glover, B., et al. (2018). *The NCAR-UWyo Aerosol Inlet*. The University of Wyoming. Retrieved from http://www-das.uwyo.edu/~jsnider/inlet_report_v02.pdf

Song, S., Gao, M., Xu, W., Shao, J., Shi, G., Wang, S., et al. (2018). Fine-particle pH for Beijing winter haze as inferred from different thermodynamic equilibrium models. *Atmospheric Chemistry and Physics*, *18*(10), 7423–7438. https://doi.org/10.5194/acp-18-7423-2018

Sorooshian, A., Murphy, S. M., Hersey, S., Gates, H., Padro, L. T., Nenes, A., et al. (2008). Comprehensive airborne characterization of aerosol from a major bovine source. *Atmospheric Chemistry and Physics*, *8*(17), 5489–5520. https://doi.org/10.5194/acp-8-5489-2008

Sorooshian, Armin, Brechtel, F. J., Ma, Y., Weber, R. J., Corless, A., Flagan, R. C., & Seinfeld, J. H. (2006). Modeling and Characterization of a Particle-into-Liquid Sampler (PILS). *Aerosol Science and Technology*, *40*(6), 396–409. https://doi.org/10.1080/02786820600632282

Staebler, R. M., McGinn, S. M., Crenna, B. P., Flesch, T. K., Hayden, K. L., & Li, S.-M. (2009). Three-dimensional characterization of the ammonia plume from a beef cattle feedlot. *Atmospheric Environment*, *43*(38), 6091–6099. https://doi.org/10.1016/j.atmosenv.2009.08.045

Stahl, C., Crosbie, E., Bañaga, P. A., Betito, G., Braun, R. A., Cainglet, Z. M., et al. (2021). Total organic carbon and the contribution from speciated organics in cloud water: airborne data analysis from the CAMP^{2}Ex field campaign. *Atmospheric Chemistry and Physics*, *21*(18), 14109–14129. https://doi.org/10.5194/acp-21-14109-2021

Stelson, A. W., & Seinfeld, J. H. (1982). Relative humidity and temperature dependence of the ammonium nitrate dissociation constant. *Atmospheric Environment (1967)*, *16*(5), 983–992. https://doi.org/10.1016/0004-6981(82)90184-6

Stelson, A. W., Friedlander, S. K., & Seinfeld, J. H. (1979a). A note on the equilibrium relationship between ammonia and nitric acid and particulate ammonium nitrate. *Atmospheric Environment (1967)*, *13*(3), 369–371. https://doi.org/10.1016/0004-6981(79)90293-2

Stelson, A. W., Friedlander, S. K., & Seinfeld, J. H. (1979b). A note on the equilibrium relationship between ammonia and nitric acid and particulate ammonium nitrate. *Atmospheric Environment (1967)*, *13*(3), 369–371. https://doi.org/10.1016/0004-6981(79)90293-2

Sullivan, A. P., Frank, N., Onstad, G., Simpson, C. D., & Collett Jr., J. L. (2011). Application of high-performance anion-exchange chromatography–pulsed amperometric detection for measuring carbohydrates in routine daily filter samples collected by a national network: 1. Determination of the impact of biomass burning in the upper Midwest. *Journal of Geophysical Research: Atmospheres*, *116*(D8). https://doi.org/10.1029/2010JD014166

Sullivan, A. P., May, A. A., Lee, T., McMeeking, G. R., Kreidenweis, S. M., Akagi, S. K., et al. (2014). Airborne characterization of smoke marker ratios from prescribed burning. *Atmospheric Chemistry and Physics*, *14*(19), 10535–10545. https://doi.org/10.5194/acp-14-10535-2014

Sullivan, A. P., Guo, H., Schroder, J. C., Campuzano-Jost, P., Jimenez, J. L., Campos, T., et al. (2019). Biomass Burning Markers and Residential Burning in the WINTER Aircraft Campaign. *Journal of Geophysical Research: Atmospheres*, *124*(3), 1846–1861. https://doi.org/10.1029/2017JD028153

Sullivan, Amy P., Pokhrel, R. P., Shen, Y., Murphy, S. M., Toohey, D. W., Campos, T., et al. (2022a). Examination of brown carbon absorption from wildfires in the western US during the WE-CAN study. *Atmospheric Chemistry and Physics*, *22*(20), 13389–13406. https://doi.org/10.5194/acp-22-13389-2022

Sullivan, Amy P., Pokhrel, R. P., Shen, Y., Murphy, S. M., Toohey, D. W., Campos, T., et al. (2022b). Examination of brown carbon absorption from wildfires in the western US during the WE-CAN study. *Atmospheric Chemistry and Physics*, *22*(20), 13389–13406. https://doi.org/10.5194/acp-22-13389-2022

Tao, Y., & Murphy, J. G. (2019). The sensitivity of $PM_{2.5}$ acidity to meteorological parameters and chemical composition changes: 10-year records from six Canadian monitoring sites. *Atmospheric Chemistry and Physics*, *19*(14), 9309–9320. https://doi.org/10.5194/acp-19-9309-2019

Tao, Y., & Murphy, J. G. (2021). Simple Framework to Quantify the Contributions from Different Factors Influencing Aerosol pH Based on NHx Phase-Partitioning Equilibrium. *Environmental Science & Technology*, *55*(15), 10310–10319. https://doi.org/10.1021/acs.est.1c03103

Tao, Y., Moravek, A., Furlani, T. C., Power, C. E., VandenBoer, T. C., Chang, R. Y.-W., et al. (2022). Acidity of Size-Resolved Sea-Salt Aerosol in a Coastal Urban Area: Comparison of Existing and New Approaches. *ACS Earth and Space Chemistry*, *6*(5), 1239–1249. https://doi.org/10.1021/acsearthspacechem.1c00367

Tian, D., & Niu, S. (2015). A global analysis of soil acidification caused by nitrogen addition. *Environmental Research Letters*, *10*(2), 024019. https://doi.org/10.1088/1748-9326/10/2/024019

Van Damme, M., Clarisse, L., Whitburn, S., Hadji-Lazaro, J., Hurtmans, D., Clerbaux, C., & Coheur, P.-F. (2018). Industrial and agricultural ammonia point sources exposed. *Nature*, *564*(7734), 99–103. https://doi.org/10.1038/s41586-018-0747-1

van Vuuren, D. P., Edmonds, J., Kainuma, M., Riahi, K., Thomson, A., Hibbard, K., et al. (2011). The representative concentration pathways: an overview. *Climatic Change*, *109*(1), 5. https://doi.org/10.1007/s10584-011-0148-z

Wang, R., Guo, X., Pan, D., Kelly, J. T., Bash, J. O., Sun, K., et al. (2021). Monthly Patterns of Ammonia Over the Contiguous United States at 2-km Resolution. *Geophysical Research Letters*, *48*(5), e2020GL090579. https://doi.org/10.1029/2020GL090579

Wexler, A. S., & Seinfeld, J. H. (1991). Second-generation inorganic aerosol model. *Atmospheric Environment. Part A. General Topics*, *25*(12), 2731–2748. https://doi.org/10.1016/0960-1686(91)90203-J

Womack, C. C., McDuffie, E. E., Edwards, P. M., Bares, R., de Gouw, J. A., Docherty, K. S., et al. (2019). An Odd Oxygen Framework for Wintertime Ammonium Nitrate Aerosol Pollution in Urban Areas: NOx and VOC Control as Mitigation Strategies. *Geophysical Research Letters*, *46*(9), 4971–4979. https://doi.org/10.1029/2019GL082028

Wyer, K. E., Kelleghan, D. B., Blanes-Vidal, V., Schauberger, G., & Curran, T. P. (2022). Ammonia emissions from agriculture and their contribution to fine particulate matter: A review of implications for human health. *Journal of Environmental Management*, *323*, 116285. https://doi.org/10.1016/j.jenvman.2022.116285

Yu, X.-Y., Lee, T., Ayres, B., Kreidenweis, S. M., Collett, J. L., & Malm, W. (2005). Particulate Nitrate Measurement Using Nylon Filters. *Journal of the Air & Waste Management Association*, *55*(8), 1100–1110. https://doi.org/10.1080/10473289.2005.10464721

Zahniser, M. S., Nelson, D. D., McManus, B., Kebabian, P. L., Lloyd, D., Fowler, D., et al. (1997). Measurement of trace gas fluxes using tunable diode laser spectroscopy. *Philosophical Transactions of the Royal Society of London. Series A: Physical and Engineering Sciences*, *351*(1696), 371–382. https://doi.org/10.1098/rsta.1995.0040

Zhan, X., Bo, Y., Zhou, F., Liu, X., Paerl, H. W., Shen, J., et al. (2017). Evidence for the Importance of Atmospheric Nitrogen Deposition to Eutrophic Lake Dianchi, China. *Environmental Science & Technology*, *51*(12), 6699–6708. https://doi.org/10.1021/acs.est.6b06135

APPENDIX A: DATA OVERVIEW

Table S1. Summary statistics of temperature, relative humidity, and measured aerosol species for all flights aggregated and per flight. Aerosol species are reported at STP (1 atm and 273.15 K). Abbreviated species (from left to right) are as follows: acetate (acet.), oxalate (oxal.), formate (form.), methanesulfonic acid (MSA), glutarate (glut.), propionate (prop.), succinate (succ.), levoglucosan (levogl.).

		T (˚C)	RH (%)	NH_4^+	SO_4^{2-}	NO_3^-	NO_2^-	Cl^-	Na^+	K^+	Mg^{2+}	Ca^{2+} (μg m^{-3})	Acet.	Oxal.	Form.	MSA	Glut.	Prop.	Succ.	Levogl.
All Flights	**mean**	22.9	39.8	0.382	0.521	0.331	0.048	0.400	0.274	0.151	0.233	0.442	1.105	0.136	0.716	0.069	0.039	0.103	0.027	0.166
	std	4.5	22.7	0.543	0.373	0.477	0.045	0.354	0.264	0.153	0.210	0.349	0.729	0.128	0.609	0.044	0.042	0.066	0.035	0.171
	min	5.2	12.5	0.001	0.008	0.004	0.001	0.002	0.003	0.003	0.004	0.003	0.003	0.002	0.003	0.002	0.001	0.001	0.001	0.004
	25%	19.9	27.2	0.089	0.231	0.049	0.016	0.144	0.098	0.051	0.101	0.211	0.529	0.042	0.217	0.037	0.013	0.052	0.007	0.070
	50%	23.0	33.0	0.181	0.472	0.116	0.031	0.300	0.197	0.105	0.172	0.351	1.033	0.090	0.537	0.062	0.025	0.095	0.017	0.121
	75%	26.2	45.2	0.427	0.730	0.376	0.071	0.540	0.361	0.196	0.286	0.570	1.540	0.198	1.103	0.094	0.052	0.141	0.036	0.186
	max	33.0	282.9	4.487	3.029	2.926	0.486	2.550	1.933	1.524	1.467	2.638	3.949	0.782	3.508	0.353	0.398	0.355	0.386	1.293
RF01	**mean**	22.1	32.1	0.281	1.039	0.267	0.056	0.254	0.119	0.050	0.103	0.225	0.215	0.246	0.224	0.053	0.085	0.029	0.042	0.140
	std	3.8	5.5	0.427	0.468	0.282	0.042	0.265	0.148	0.046	0.053	0.135	0.157	0.193	0.152	0.018	0.049	0.019	0.027	0.055
	min	15.1	24.6	0.001	0.493	0.015	0.009	0.002	0.003	0.003	0.007	0.049	0.022	0.027	0.084	0.020	0.033	0.001	0.001	0.065
	25%	19.7	28.1	0.023	0.708	0.049	0.037	0.103	0.036	0.022	0.068	0.121	0.119	0.063	0.115	0.040	0.042	0.013	0.022	0.105
	50%	22.9	30.6	0.130	0.917	0.221	0.057	0.179	0.063	0.034	0.092	0.211	0.160	0.201	0.174	0.051	0.064	0.028	0.034	0.121
	75%	25.4	34.1	0.321	1.299	0.371	0.061	0.306	0.139	0.053	0.139	0.277	0.251	0.377	0.240	0.067	0.125	0.041	0.069	0.167
	max	26.8	46.1	2.007	3.029	1.555	0.283	1.446	0.560	0.188	0.228	0.676	0.733	0.697	0.622	0.100	0.196	0.078	0.091	0.310

		T (˚C)	RH (%)	NH_4^+	SO_4^{2-}	NO_3^-	NO_2^-	Cl^-	Na^+	K^+	Mg^{2+}	Ca^{2+} (µg m^{-3})	Acet.	Oxal.	Form.	MSA	Glut.	Prop.	Succ.	Levogl.
RF02	**mean**	19.9	50.9	0.587	0.419	0.250	0.065	0.413	0.194	0.077	0.324	0.348	1.261	0.263	0.570	0.085	0.043	0.123	0.036	0.180
	std	3.5	10.8	0.880	0.269	0.264	0.042	0.407	0.139	0.076	0.225	0.279	0.565	0.138	0.347	0.029	0.022	0.078	0.018	0.096
	min	11.6	27.3	0.005	0.012	0.022	0.007	0.042	0.013	0.005	0.048	0.046	0.060	0.060	0.058	0.029	0.008	0.004	0.004	0.043
	25%	17.2	43.8	0.083	0.168	0.046	0.027	0.163	0.081	0.031	0.183	0.192	0.862	0.127	0.303	0.069	0.030	0.068	0.021	0.119
	50%	21.0	51.1	0.260	0.415	0.140	0.068	0.307	0.176	0.058	0.279	0.291	1.151	0.281	0.490	0.087	0.041	0.103	0.038	0.165
	75%	23.0	57.4	0.655	0.619	0.321	0.104	0.517	0.290	0.098	0.400	0.408	1.542	0.380	0.765	0.105	0.051	0.156	0.051	0.210
	max	25.5	75.3	4.487	0.975	1.074	0.139	2.550	0.645	0.532	1.299	1.932	2.810	0.498	1.562	0.149	0.105	0.355	0.071	0.606
RF03	**mean**	24.2	31.5	0.557	0.210	0.054	0.020	0.368	0.292	0.195	0.268	0.568	1.531	0.084	0.784	0.067	0.020	0.119	0.043	0.173
	std	3.3	18.7	0.699	0.156	0.027	0.010	0.312	0.277	0.250	0.186	0.434	0.682	0.037	0.606	0.028	0.012	0.052	0.025	0.067
	min	14.3	22.6	0.013	0.056	0.023	0.005	0.036	0.004	0.003	0.044	0.082	0.012	0.018	0.019	0.003	0.005	0.017	0.009	0.066
	25%	22.6	25.1	0.119	0.120	0.037	0.010	0.160	0.110	0.066	0.128	0.318	1.108	0.062	0.353	0.054	0.012	0.080	0.024	0.126
	50%	25.6	26.2	0.230	0.170	0.047	0.018	0.254	0.205	0.120	0.220	0.442	1.595	0.084	0.668	0.069	0.017	0.119	0.040	0.163
	75%	26.5	32.1	0.650	0.242	0.060	0.029	0.480	0.355	0.246	0.354	0.617	1.965	0.095	1.072	0.085	0.025	0.161	0.056	0.202
	max	27.6	150.3	2.938	0.977	0.174	0.045	1.521	1.330	1.524	0.934	2.638	2.981	0.211	2.505	0.129	0.068	0.216	0.126	0.352
RF06	**mean**	23.1	31.8	0.402	0.446	0.057	0.035	0.409	0.262	0.249	0.265	0.412	1.740	0.182	1.084	0.104	0.050	0.169	0.028	0.432
	std	2.1	26.1	0.526	0.276	0.055	0.059	0.284	0.216	0.136	0.162	0.230	0.858	0.127	0.779	0.036	0.043	0.060	0.021	0.331
	min	18.8	12.5	0.005	0.065	0.004	0.004	0.010	0.024	0.053	0.010	0.032	0.003	0.020	0.021	0.011	0.003	0.002	0.001	0.062
	25%	21.5	26.6	0.072	0.244	0.035	0.014	0.192	0.116	0.148	0.145	0.240	1.043	0.055	0.442	0.083	0.013	0.118	0.013	0.140
	50%	22.7	29.0	0.139	0.450	0.039	0.023	0.328	0.205	0.234	0.227	0.368	1.796	0.159	1.020	0.110	0.045	0.183	0.025	0.208

		T (˚C)	RH (%)	NH_4^+	SO_4^{2-}	NO_3^-	NO_2^-	Cl^-	Na^+	K^+	Mg^{2+}	Ca^{2+} (µg m^{-3})	Acet.	Oxal.	Form.	MSA	Glut.	Prop.	Succ.	Levogl.
	75%	24.9	33.1	0.541	0.572	0.055	0.032	0.643	0.353	0.338	0.365	0.530	2.383	0.301	1.573	0.125	0.079	0.207	0.037	0.728
	max	27.1	242.3	2.005	1.345	0.364	0.486	1.079	1.123	0.743	0.803	1.201	3.949	0.418	3.054	0.201	0.252	0.334	0.120	1.293
RF08	**mean**	18.2	79.2	0.375	0.678	0.906	0.091	0.282	0.219	0.137	0.225	0.194	1.458	0.112	0.832	0.086	0.017	0.108	0.009	0.167
	std	1.6	24.8	0.229	0.238	0.538	0.044	0.193	0.231	0.120	0.140	0.118	0.573	0.069	0.514	0.043	0.013	0.049	0.005	0.113
	min	14.2	60.9	0.071	0.198	0.034	0.006	0.024	0.004	0.011	0.073	0.003	0.005	0.012	0.003	0.003	0.003	0.004	0.002	0.030
	25%	17.3	71.7	0.215	0.528	0.393	0.059	0.102	0.065	0.060	0.143	0.134	1.157	0.066	0.384	0.052	0.009	0.075	0.006	0.074
	50%	18.3	76.9	0.363	0.723	1.012	0.099	0.260	0.157	0.100	0.186	0.175	1.463	0.117	0.804	0.080	0.013	0.105	0.008	0.141
	75%	19.2	82.0	0.452	0.820	1.314	0.120	0.409	0.256	0.158	0.255	0.229	1.923	0.138	1.278	0.120	0.022	0.135	0.011	0.221
	max	21.6	282.9	1.294	1.414	1.923	0.196	0.724	1.130	0.604	0.854	0.676	2.675	0.550	1.731	0.174	0.072	0.199	0.031	0.448
RF09	**mean**	24.1	44.3	0.311	0.482	0.087	0.052	0.309	0.170	0.092	0.237	0.382	0.936	0.030	0.846	0.046	0.021	0.073	0.021	0.160
	std	3.4	5.3	0.461	0.243	0.051	0.042	0.266	0.126	0.067	0.260	0.263	0.466	0.025	0.584	0.020	0.021	0.038	0.062	0.131
	min	17.4	34.6	0.010	0.067	0.024	0.002	0.033	0.006	0.017	0.035	0.029	0.021	0.003	0.015	0.007	0.002	0.006	0.002	0.011
	25%	21.3	39.9	0.148	0.293	0.042	0.010	0.109	0.087	0.046	0.091	0.196	0.637	0.013	0.383	0.033	0.008	0.048	0.003	0.065
	50%	25.4	44.9	0.204	0.491	0.093	0.045	0.231	0.157	0.075	0.167	0.322	0.948	0.024	0.835	0.042	0.014	0.070	0.005	0.099
	75%	26.7	48.0	0.270	0.646	0.113	0.093	0.412	0.207	0.120	0.267	0.502	1.220	0.037	1.299	0.060	0.031	0.101	0.014	0.252
	max	28.9	53.0	2.735	0.997	0.266	0.123	1.048	0.613	0.317	1.467	1.027	1.962	0.119	2.316	0.089	0.122	0.153	0.372	0.534
RF11	**mean**	26.0	37.4	0.332	0.390	0.099	0.023	0.300	0.247	–	0.212	0.430	0.763	0.066	1.018	0.048	0.015	0.074	0.013	0.128
	std	2.3	17.9	0.418	0.291	0.064	0.017	0.344	0.264	–	0.195	0.256	0.397	0.058	0.477	0.025	0.014	0.038	0.021	0.090
	min	21.1	26.3	0.005	0.015	0.033	0.002	0.011	0.015	–	0.017	0.014	0.003	0.003	0.126	0.002	0.002	0.003	0.001	0.019

		T (˚C)	RH (%)	NH_4^+	SO_4^{2-}	NO_3^-	NO_2^-	Cl^-	Na^+	K^+	Mg^{2+}	Ca^{2+} (µg m^{-3})	Acet.	Oxal.	Form.	MSA	Glut.	Prop.	Succ.	Levogl.
	25%	24.3	31.1	0.126	0.132	0.055	0.009	0.093	0.098	–	0.117	0.212	0.491	0.024	0.673	0.031	0.007	0.047	0.004	0.060
	50%	26.5	36.2	0.179	0.271	0.079	0.018	0.208	0.199	–	0.169	0.380	0.836	0.044	1.017	0.047	0.012	0.069	0.006	0.109
	75%	27.8	38.2	0.360	0.691	0.132	0.034	0.340	0.310	–	0.223	0.624	1.042	0.106	1.317	0.065	0.017	0.111	0.010	0.178
	max	29.5	169.9	2.790	0.950	0.395	0.077	1.811	1.929	–	1.329	1.225	1.687	0.287	2.306	0.097	0.065	0.152	0.122	0.555
RF12	**mean**	19.3	30.1	0.279	0.565	0.416	0.050	0.620	0.439	–	0.198	0.766	0.802	0.168	0.641	0.055	0.050	0.090	0.025	0.106
	std	3.6	5.0	0.398	0.417	0.303	0.042	0.438	0.374	–	0.279	0.481	0.751	0.129	0.832	0.052	0.033	0.067	0.032	0.070
	min	5.2	17.7	0.056	0.114	0.040	0.006	0.032	0.021	–	0.004	0.088	0.060	0.018	0.015	0.002	0.003	0.009	0.001	0.004
	25%	18.4	27.9	0.120	0.289	0.171	0.021	0.249	0.135	–	0.044	0.407	0.250	0.068	0.085	0.019	0.028	0.043	0.009	0.054
	50%	20.3	29.8	0.171	0.490	0.332	0.040	0.545	0.352	–	0.097	0.656	0.542	0.180	0.200	0.039	0.042	0.064	0.016	0.081
	75%	21.6	31.6	0.264	0.683	0.643	0.060	0.932	0.632	–	0.215	1.056	1.169	0.230	0.938	0.071	0.065	0.125	0.026	0.142
	max	23.4	59.4	3.002	2.834	1.207	0.228	1.876	1.933	–	1.431	2.303	3.500	0.719	3.508	0.279	0.165	0.303	0.179	0.285
RF13	**mean**	25.2	34.0	0.539	0.780	0.836	0.060	0.525	0.428	0.208	0.292	0.539	0.954	0.138	0.436	0.058	0.031	0.106	0.018	0.098
	std	1.8	8.6	0.607	0.447	0.937	0.047	0.415	0.306	0.142	0.268	0.382	0.562	0.102	0.353	0.036	0.026	0.071	0.014	0.053
	min	17.2	19.5	0.020	0.191	0.035	0.005	0.030	0.031	0.005	0.018	0.058	0.007	0.012	0.031	0.003	0.003	0.003	0.001	0.009
	25%	24.3	27.3	0.087	0.362	0.053	0.018	0.244	0.237	0.112	0.089	0.267	0.605	0.041	0.138	0.027	0.014	0.065	0.005	0.061
	50%	25.2	32.7	0.244	0.794	0.223	0.051	0.438	0.394	0.177	0.182	0.439	0.967	0.104	0.359	0.049	0.023	0.084	0.019	0.087
	75%	26.2	43.0	0.782	1.160	1.737	0.098	0.720	0.481	0.267	0.429	0.727	1.299	0.233	0.557	0.090	0.044	0.142	0.025	0.136
	max	28.6	45.5	2.621	1.924	2.926	0.212	1.922	1.601	0.569	1.152	1.728	2.343	0.355	1.356	0.141	0.153	0.286	0.060	0.241
RF14	**mean**	29.3	19.8	0.100	0.430	0.258	0.029	0.428	0.284	–	0.150	0.400	0.753	0.061	0.518	0.067	0.069	0.082	0.036	0.043

	T (˚C)	RH (%)	NH_4^+	SO_4^{2-}	NO_3^-	NO_2^-	Cl^-	Na^+	K^+	Mg^{2+}	Ca^{2+}	Acet.	Oxal.	Form.	MSA	Glut.	Prop.	Succ.	Levogl.
											($\mu g\ m^{-3}$)								
std	3.5	3.3	0.227	0.297	0.202	0.028	0.327	0.216	–	0.134	0.244	0.471	0.104	0.454	0.068	0.082	0.056	0.071	0.036
min	21.3	13.6	0.003	0.008	0.004	0.001	0.005	0.022	–	0.006	0.006	0.008	0.002	0.009	0.003	0.001	0.002	0.002	0.004
25%	27.3	17.1	0.029	0.235	0.119	0.011	0.203	0.117	–	0.064	0.212	0.316	0.018	0.112	0.030	0.014	0.045	0.005	0.015
50%	30.8	20.2	0.048	0.377	0.192	0.019	0.339	0.193	–	0.100	0.364	0.718	0.038	0.397	0.042	0.061	0.065	0.010	0.032
75%	31.8	21.6	0.094	0.565	0.382	0.037	0.692	0.431	–	0.181	0.557	1.007	0.063	0.765	0.071	0.079	0.112	0.023	0.058
max	33.0	27.4	1.679	1.481	0.992	0.137	1.299	0.802	–	0.713	1.020	1.947	0.782	1.821	0.353	0.398	0.296	0.386	0.149

APPENDIX B: MODEL INPUT SENSITIVITY TESTS

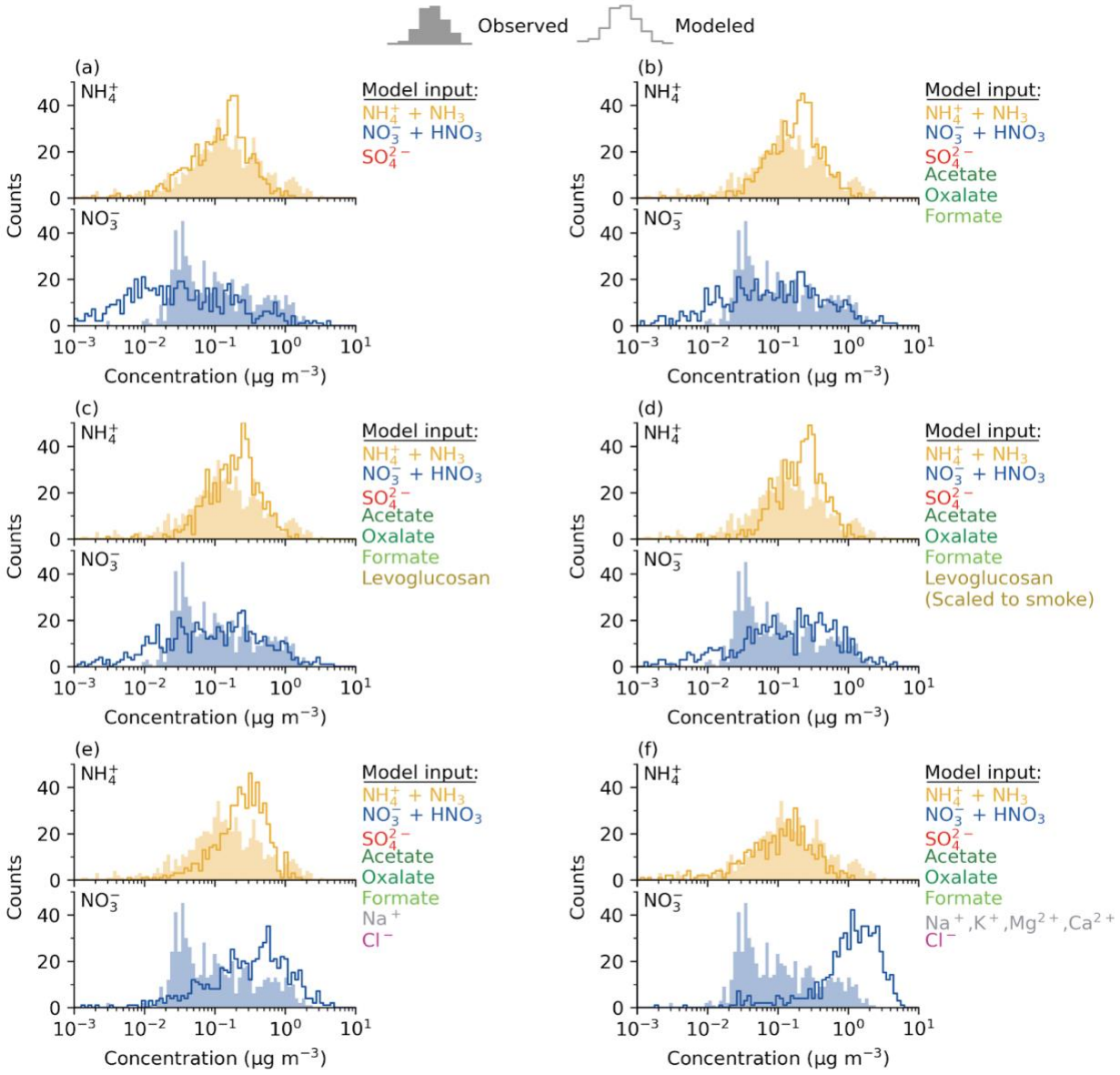

Figure S1. Model vs observed NH_4^+ (yellow) and NO_3^- (blue) from all near-source flights for various model input configurations. See Figure S2 for detail on the calculation for Levoglucosan (scaled to smoke).

For sensitivity tests with non-volatile cations (NVCs), we use E-AIM Model IV to model a H_2O-SO_4^{2-}-NO_3^--NH_4^+-Na^+-Cl^- aerosol system and include NVCs added as equivalent Na^+. E-AIM Model IV is restricted to relative humidities above 60%, but most observations during TRANS^{2}Am are made below 60% RH. Artificially inflated RH in the model (especially above the deliquescence relative humidity (DRH) of NH_4NO_3) will increase aerosol water uptake and create a model bias overestimating partitioning to the aerosol phase. We isolate and remove the effect of the RH restriction by running E-AIM Model II (without NVCs and Cl^-) once at the observed RH and once at the model-restricted $\geq$ 60% RH.

Model-observation agreement does not improve when Cl^- is included and drastically worsens when NVCs are included. Local Cl^- contribution from sea salt aerosols is negligible because the study region is landlocked (Figure 1), and including Cl^- in aerosol thermodynamics calculations does not improve model-observation agreement of NH_4^+ and NO_3^-. Including non-volatile cations in the aerosol model causes NO_3^- to be severely overpredicted to balance the influx of positive charges from NVCs. Aerosol NVCs are typically associated with dust or SSA and because of negligible marine influence in the study region, this suggests that NVCs are balanced by unmeasured dust-related anions such as carbonate and/or externally mixed.

Phase I of TRANS^{2}Am took place during an active wildfire season, and we use satellite imagery from NASA Worldview (https://worldview.earthdata.nasa.gov/) and identify 8 of the 10 flights to have occurred on smoke-impacted days. Levoglucosan is a product of cellulose pyrolysis, so it is commonly used as a tracer for biomass burning. Levoglucosan is a moderately hydrophilic organic compound (κ = 0.21; Petters and Kreidenweis, 2007), so it should promote aerosol water uptake and enhanced aerosol-phase ammonium and nitrate. Including levoglucosan in the aerosol

thermodynamic model does promote aerosol water uptake, however, does not significantly improve model-observation agreement (Figure S1 panel c).

Higher concentrations of carbon monoxide on smoke-influenced days are well-correlated with PM_3 volume concentration measurements made by the PCASP ($r = 0.81$), whereas the PILS mass concentration-derived PM_1 volume concentration is not ($r = 0.22$) well-correlated (Figure S2). This suggests that there are unmeasured smoke-related particulates between 1-3 μm in diameter. We assume this differential volume concentration between PM_1 and PM_3 to be non-polar, hydrophilic organic compounds and artificially add the corresponding amount of levoglucosan into the model by assuming the densities of organics, NVCs, and other inorganic compounds are 1.2 g cm^{-3}, 2.1 g cm^{-3}, and 1.7 g cm^{-3}, respectively (Figure S3). However, model-observation agreement of NH_4^+ and NO_3^- do not improve (Figure S1 panel d), suggesting that the inorganic partitioning of NH_x and TNO_3 is sufficiently explained by a H_2O-SO_4^{2-}-NO_3^--NH_4^+-formate-oxalate-acetate system.

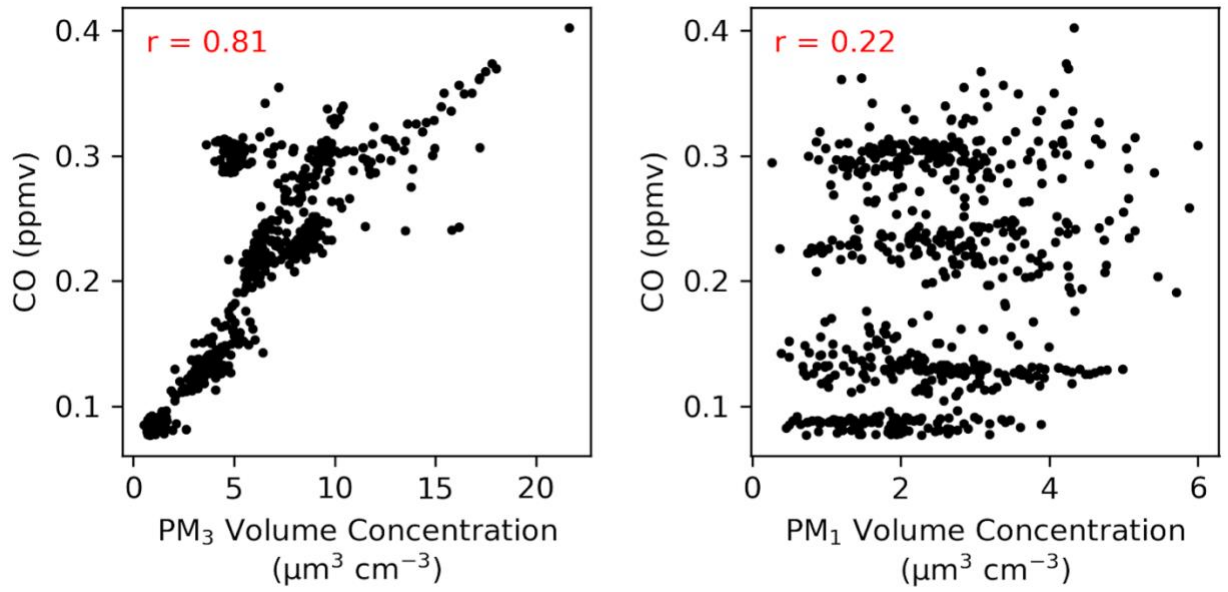

Figure S2. PM_3 volume concentration measured by the PCASP vs CO concentration (left) and PM_1 volume concentration estimated from submicron aerosol mass concentrations measured by the PILS vs CO concentration (right). Correlation coefficients shown in red.

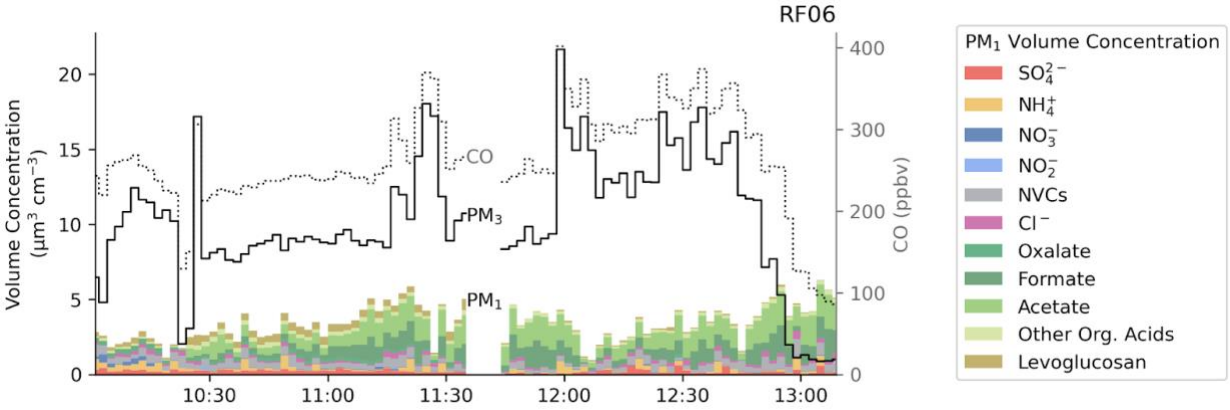

Figure S3. Example time series of PM_1 dry volume concentration estimated from PILS species (color), PM_3 dry volume concentration from PCASP (solid black line), and CO mixing ratio (dotted black line) on the right y-axis. The difference between PM_3 and PM_1 volume concentrations may be black carbon or unmeasured large organics. For the sensitivity test, this difference is attributed to unmeasured large, levoglucosan-like hydrophilic organics.

APPENDIX C: MODEL-OBSERVATION VARIANCE ANALYSIS

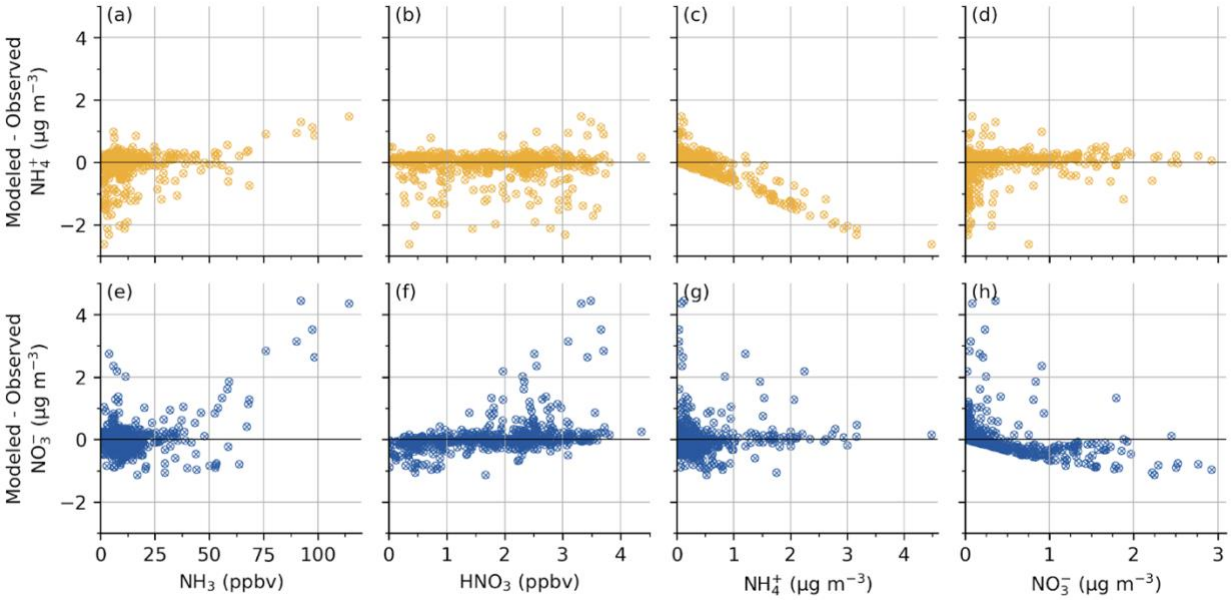

Figure S4. Variance analysis of model-observation error in predicted NH_4^+ (top row) and NO_3^- (bottom row) for NH_3, HNO_3, NH_4^+, and NO_3^- (left to right).

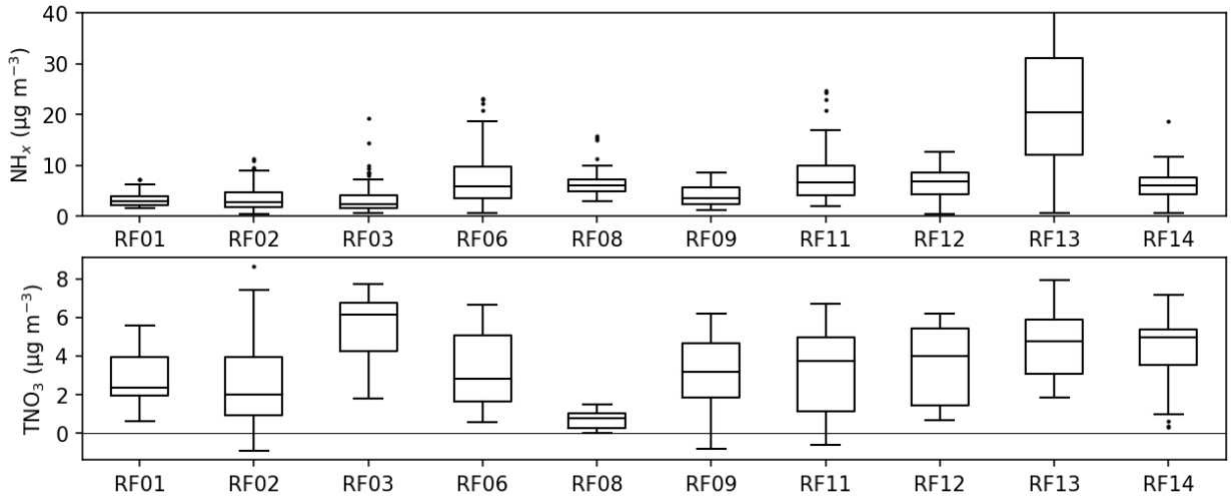

Figure S5. Box-and-whisker plots for total ammonia (top) and total nitrate (bottom) by fight. Tails represent 1.5*IQR. The upper tail for NH_x on RF13 is 59 μg m^{-3} and not shown. Lower tails for TNO_3 below 0 represent instrument noise.

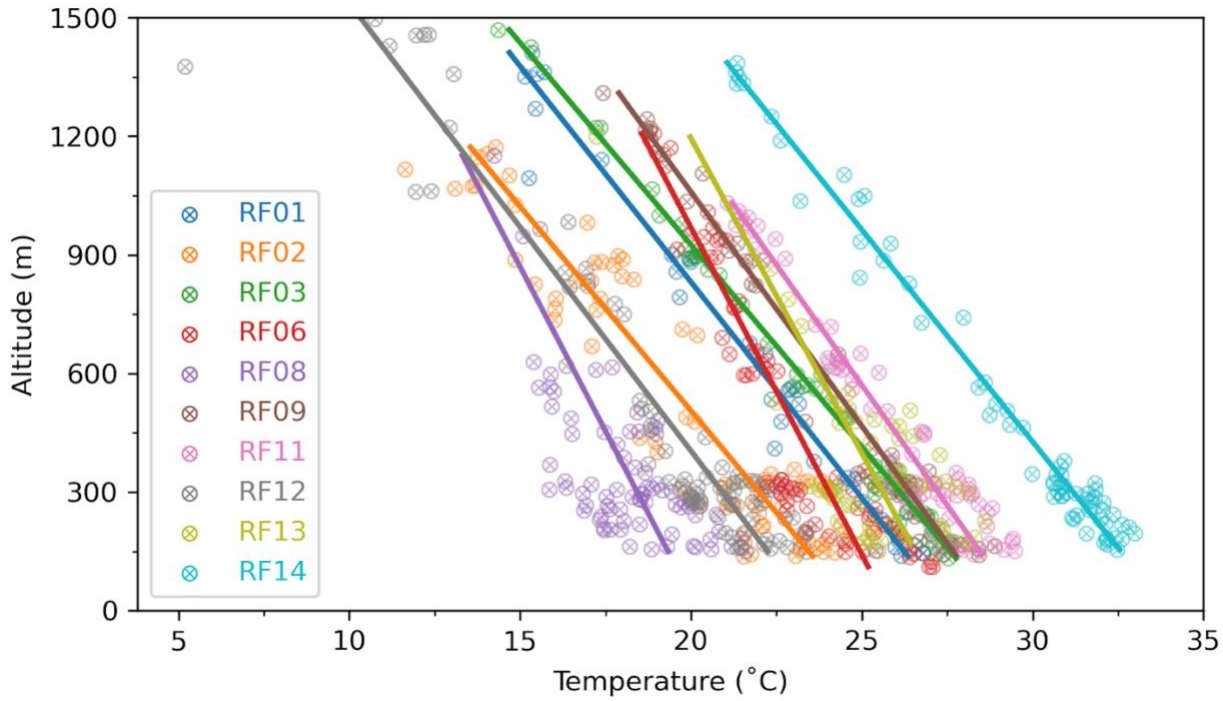

Figure S6. Temperature profiles colored by flight. Lines represent ordinary least squares fits.

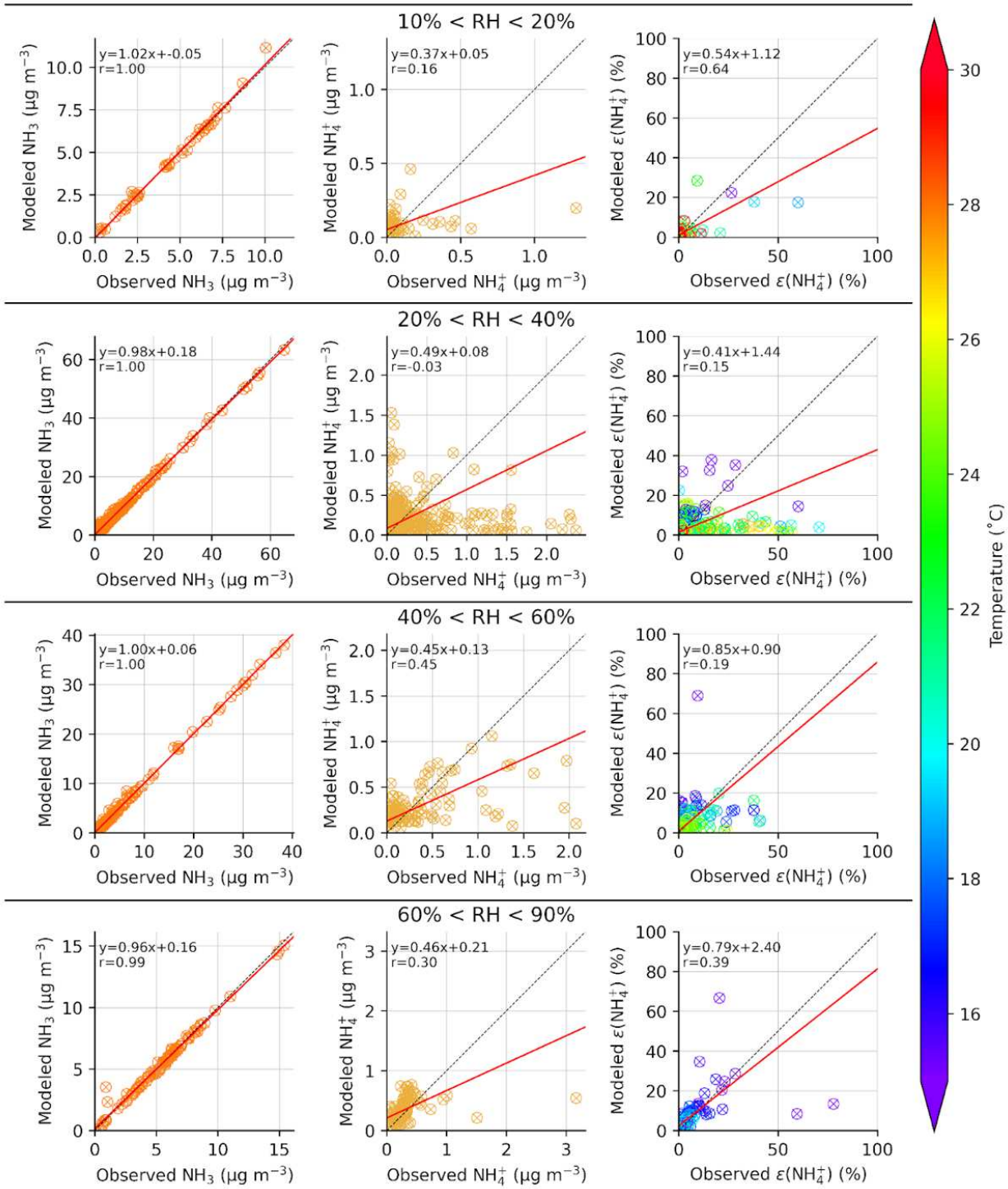

Figure S7. Model vs observed NH_3 (left), NH_4^+ (center), and total ammonia partitioning $\varepsilon(NH_4^+)$ (right) by RH bin (row) and colored by temperature. Red line represents orthogonal least squares fit.

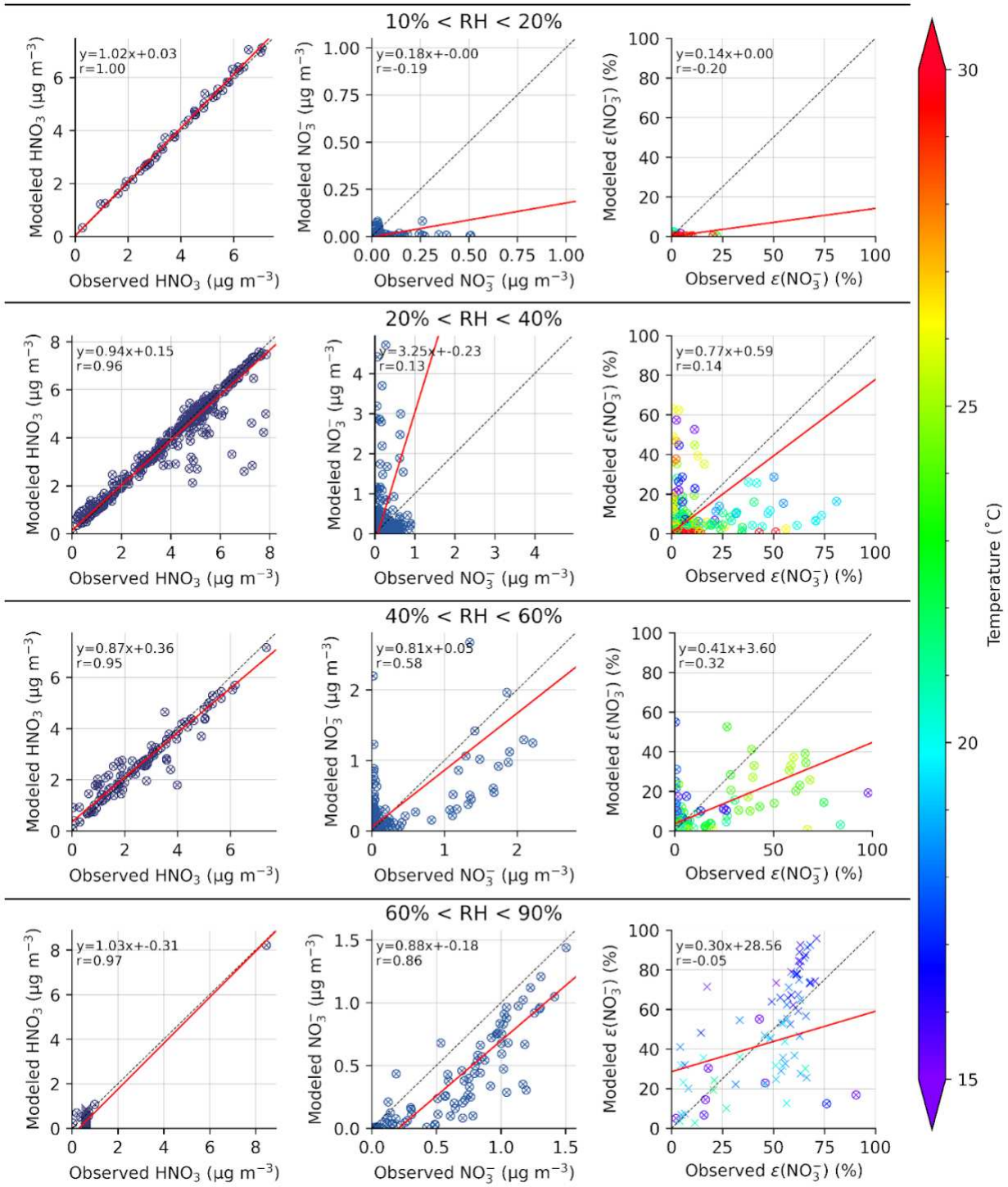

Figure S8. Model vs observed HNO_3 (left), NO_3^- (center), and total nitrate partitioning $\varepsilon(NO_3^-)$ (right) by RH bin (row) and colored by temperature. Red line represents orthogonal least squares fit. Missing HNO_3 measurements in RF08 are denoted by 'x' symbols, set to ½ LOD (½ 555 ppbv), and included in the OLS fits.

APPENDIX D: SENSITIVITY OF MODELED NH_4NO_3 TO TEMPERATURE AND RELATIVE HUMIDITY

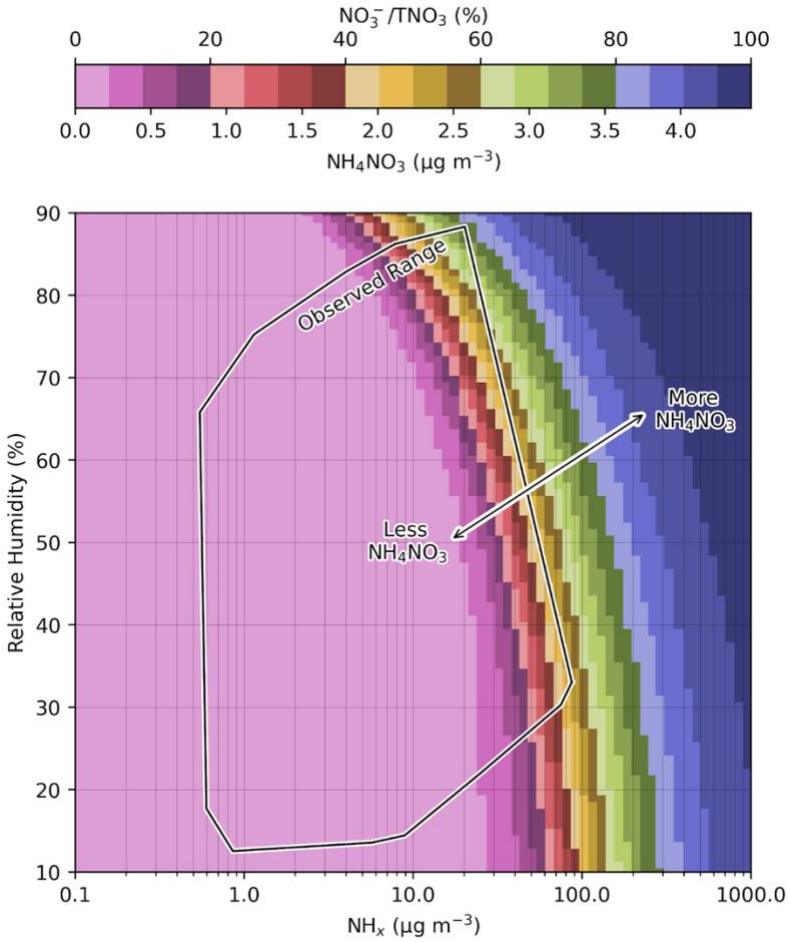

Figure S9. Modeled NH_4NO_3 and total nitrate partitioning (colorbar) for a sulfate-nitrate-ammonium system with fixed total nitrate, total sulfate, and temperature for a range of relative humidity and total ammonia concentrations. Temperature and TNO_3 are set to median observed values (25˚C, 3.53 µg m^{-3} TNO_3). The black outline shows the observed range of relative humidities and NH_x during TRANS²Am.

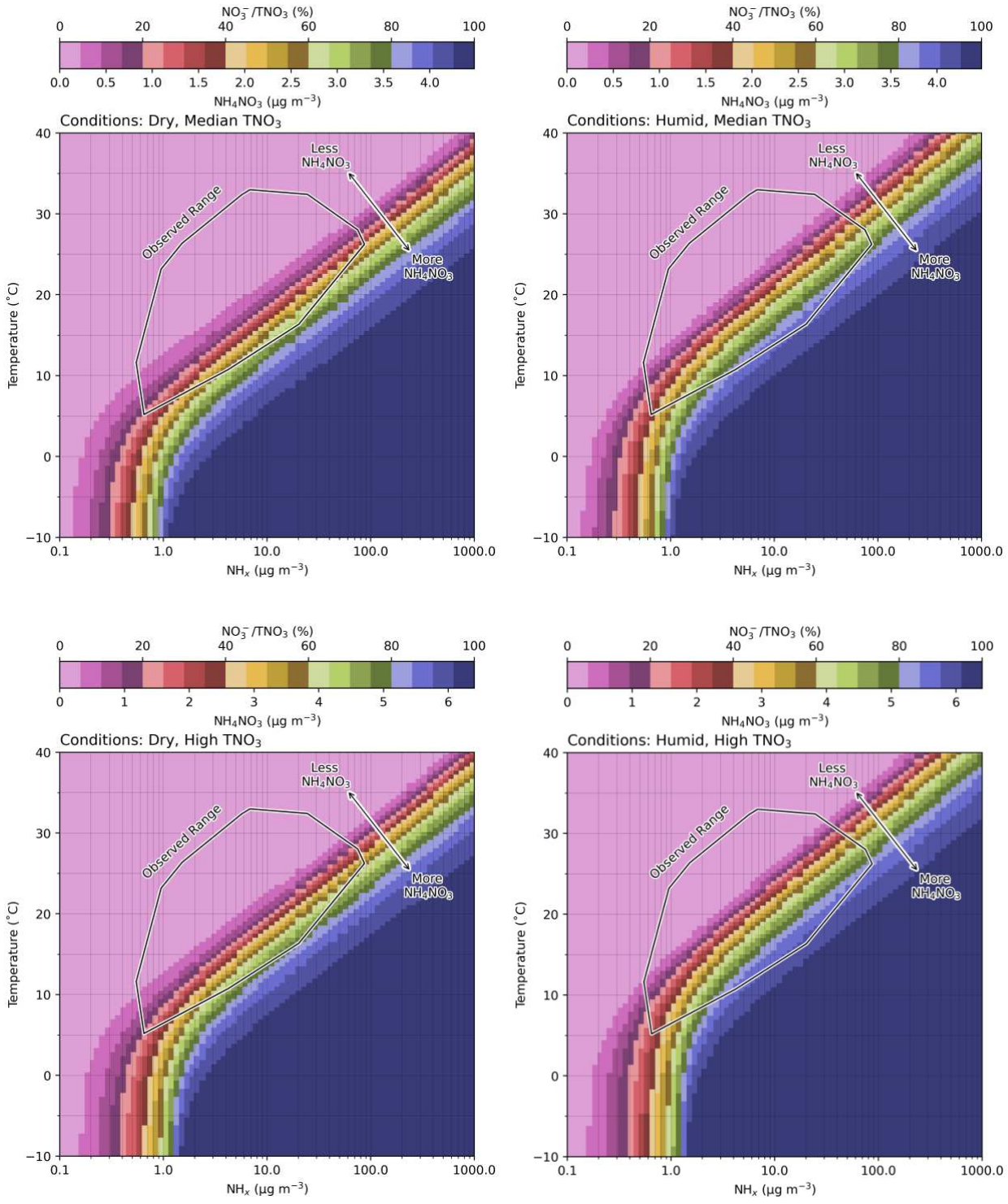

Figure S10. Same as Fig. 7 but for different TNO_3 (row) and RH (column) conditions. For TNO_3, high = 75th percentile of observed concentrations. Color represents modeled NH_4NO_3 and total nitrate partitioning for a sulfate-nitrate-ammonium system with fixed total nitrate, total sulfate, and RH for a range of temperatures and total ammonia concentrations. The range of temperatures and NH_x observed during TRANS²Am is outlined by the red dotted line.

Table S2. Percent of observations in modeled NO_3^-/TNO_3 bins in temperature vs NH_x space for dry (RH = 33%) vs humid (RH = 70%) and median observed TNO_3 (3.53 µg m^{-3}) vs high observed TNO_3. Fraction of observations in parenthesis.

Modeled NO_3^-/TNO_3	Dry		Humid	
	Median TNO_3	**High TNO_3**	**Median TNO_3**	**High TNO_3**
0-5%	70% (448/642)	64% (411/642)	45% (291/642)	37% (236/642)
5-20%	22% (141/642)	20% (126/642)	18% (117/642)	16% (105/642)
20-40%	6% (40/642)	10% (65/642)	13% (82/642)	15% (97/642)
40-60%	1% (9/642)	5% (34/642)	13% (85/642)	12% (77/642)
60-80%	1% (4/642)	1% (6/642)	10% (61/642)	17% (109/642)
80-100%	0% (0/642)	0% (0/642)	1% (6/642)	3% (18/642)

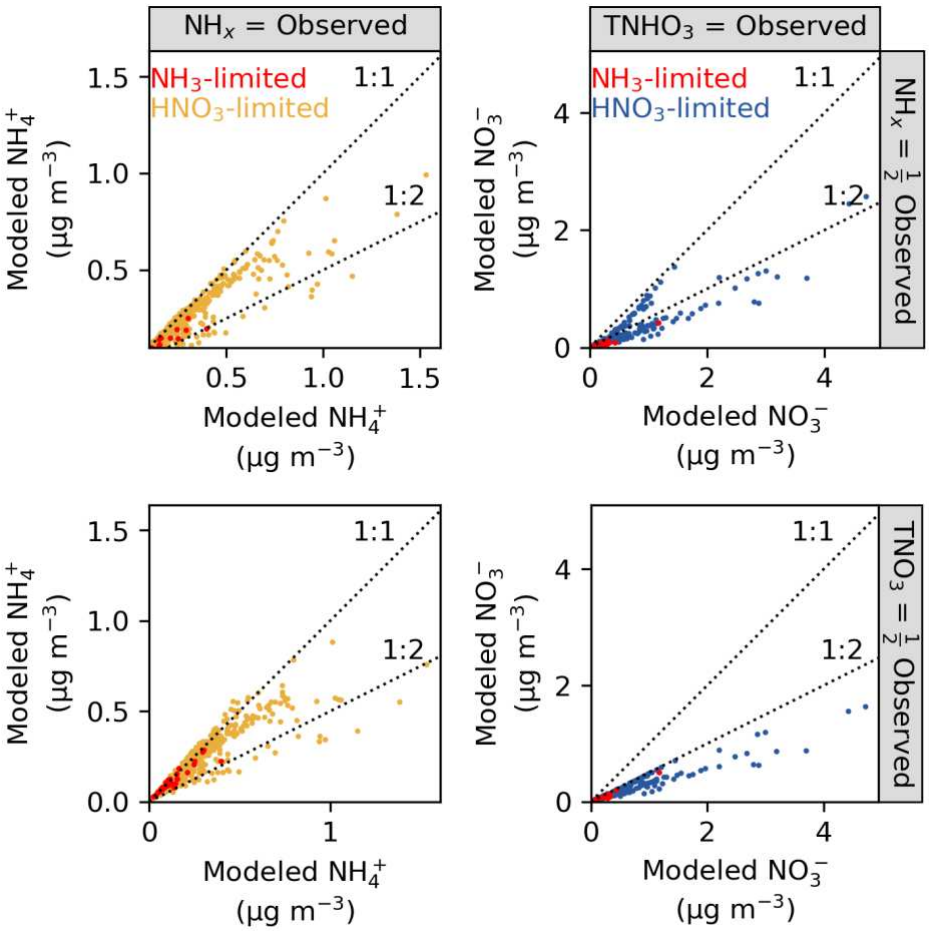

Figure S11. Sensitivity test of modeled NH_4^+ (left) and modeled NO_3^- (right) for when model input NH_x = observed and TNO_3 = observed (x-axis) vs model input NH_x = ½ observed (y-axis top row) and model input TNO_3 = ½ observed (y-axis bottom row). Data points in the NH_3-limited NH_4NO_3 formation regime are red.

APPENDIX E: KINETIC MASS TRANSFER MODELING SENSITIVITY TESTS

Table S2 shows the parameters we use to model potential evaporation of NH_4NO_3 in the aerosol inlet line on the UWKA based on kinetic mass transfer equations described in Dahneke (1983) and NH_4NO_3 equilibrium constants based on Stelson and Seinfeld (1982). We assume a closed system of NH_3 and HNO_3 that is allowed to condense and evaporate between a monodisperse aerosol population of dry NH_4NO_3 particles over time.

Table S3: Kinetic mass transfer model parameters

Parameter	Value	
Initial NH_3 concentration	50	$\mu g\ m^{-3}$
Initial HNO_3 concentration	2.5	$\mu g\ m^{-3}$
Initial aerosol diameter	1×10^{-7}	m
Number concentration	1×10^{9}	m^{-3}
Particle phase density	1700	$kg\ m^{-3}$
Accommodation Coefficient	1	[unitless]
Gas-phase diffusivity	1×10^{-5}	$m^2\ s^{-1}$
Surface tension	0.079	$N\ m^{-1}$

Figure S10 shows an example of NH_3 and HNO_3 concentrations changing over time from an ambient temperature of 20˚C to an aircraft cabin temperature of 35˚C. The blue line represents an initial NH_3 and HNO_3 concentration representative of TRANS^{2}Am conditions reaching gas-particle equilibrium over an hour to simulate the ambient environment. The red line represents NH_3 and HNO_3 concentrations in an air parcel in warmer temperatures in the aerosol inlet line on the UWKA. Panel (b) is zoomed in on the time of the temperature perturbation, and the dashed

black lines represent the time to reach half of the change in equilibrium NH_3 and HNO_3 concentrations. We use this time to assess whether significant NH_4NO_3 evaporation has occurred in the aerosol inlet line.

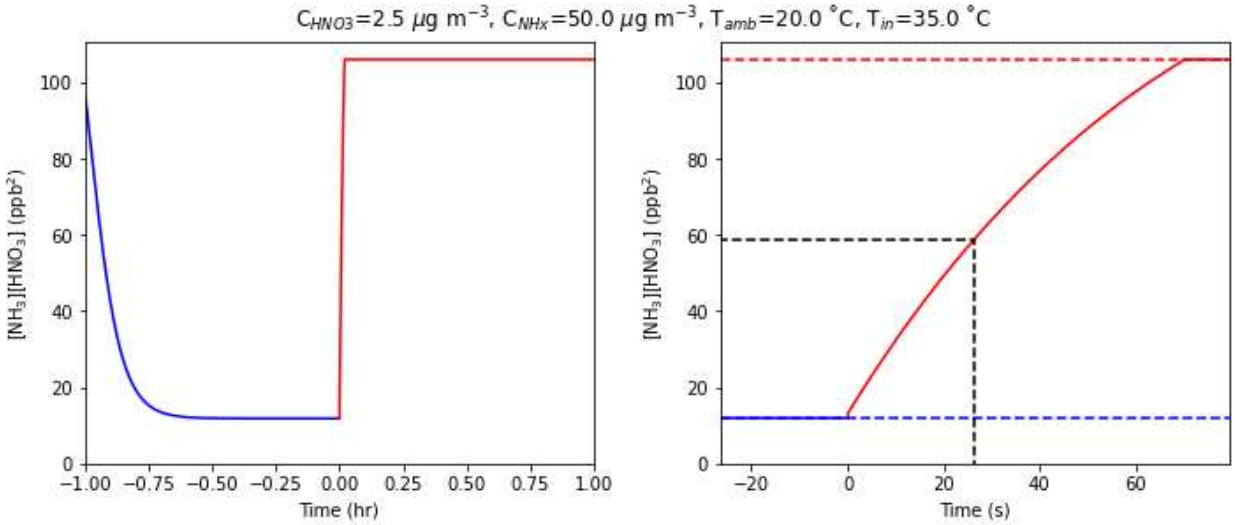

Figure S12. Example of modeled $[NH_3][HNO_3]$ concentrations over time for a given temperature perturbation. The Blue line represents an ambient temperature of 20˚C, and the red line represents an aircraft cabin temperature of 35˚C. Dashed red and blue lines represent equilibrium $[NH_3][HNO_3]$, and dashed black lines represent time to reach ½ change in equilibrium concentrations.

Figure S11 shows the time to reach a ½ change to equilibrium $[NH_3][HNO_3]$ and the change in equilibrium $[NH_3][HNO_3]$ for a range of ambient-inlet temperature gradients. The transit time in the PILS inlet is < 2 seconds, so significant NH_4NO_3 evaporation in the aerosol inlet line would be reflected by a time to reach ½ change in equilibrium $[NH_3][HNO_3]$ in less than 2 seconds (blue region in the left plot) as well as a large change in equilibrium $[NH_3][HNO_3]$ (red region in the right plot). Within the 15˚C to 25˚C range of ambient temperatures observed during TRANS^{2}Am (Table S1), the aerosol inlet temperature in the aircraft cabin would have to exceed 35˚C for significant NH_4NO_3 evaporation to occur. Cabin temperature was not measured so there is no way of verifying the aerosol inlet temperature, but a cabin temperature greater than 35˚C dangerously high and unlikely. Thus, the evaporation of NH_4NO_3 due to an ambient-aircraft temperature gradient is likely not a large source of uncertainty in our thermodynamic modeling.

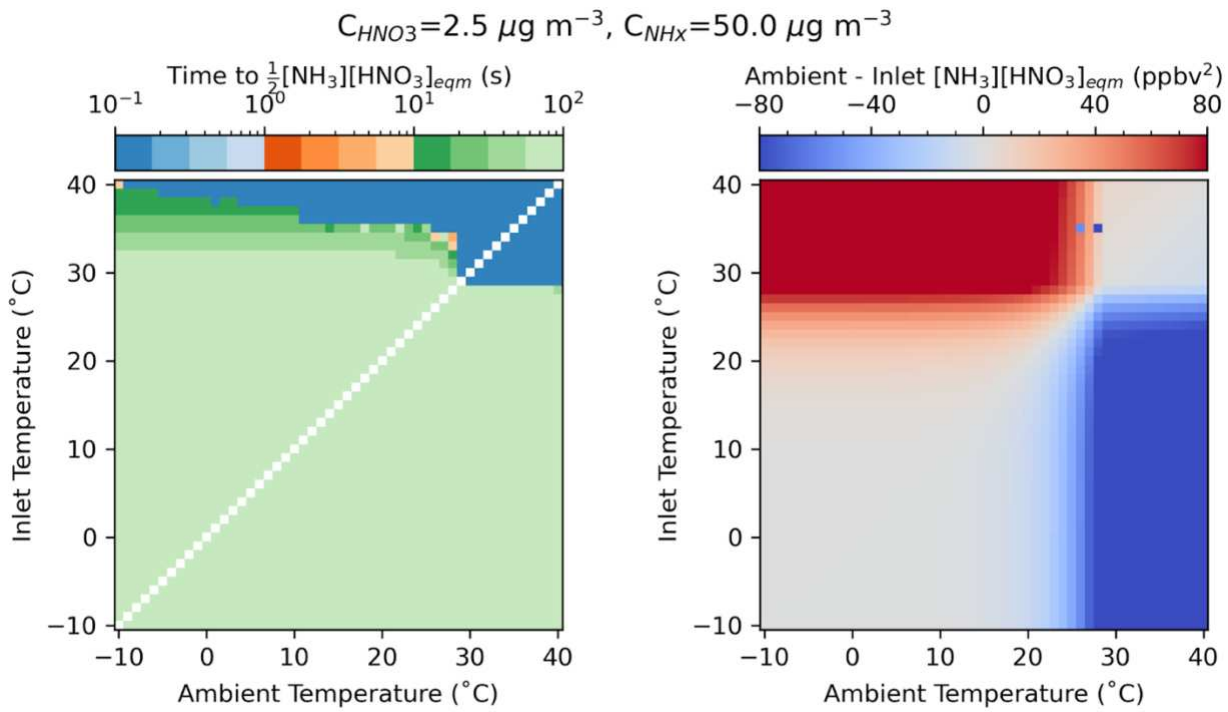

Figure S13. Calculated time to reach 50% change in equilibrium [NH_3][HNO_3] (left) and difference in equilibrium [NH_3][HNO_3] (right) for a range of gradients between ambient temperature and PILS inlet temperature. Calculated using average observed HNO_3 (2.5 µg m^{-3}), NH_3 (50 µg m^{-3}), and pressure (850 hPa).

APPENDIX F: SEASONALITY OF NH_4NO_3 IN AND OUT OF PLUMES

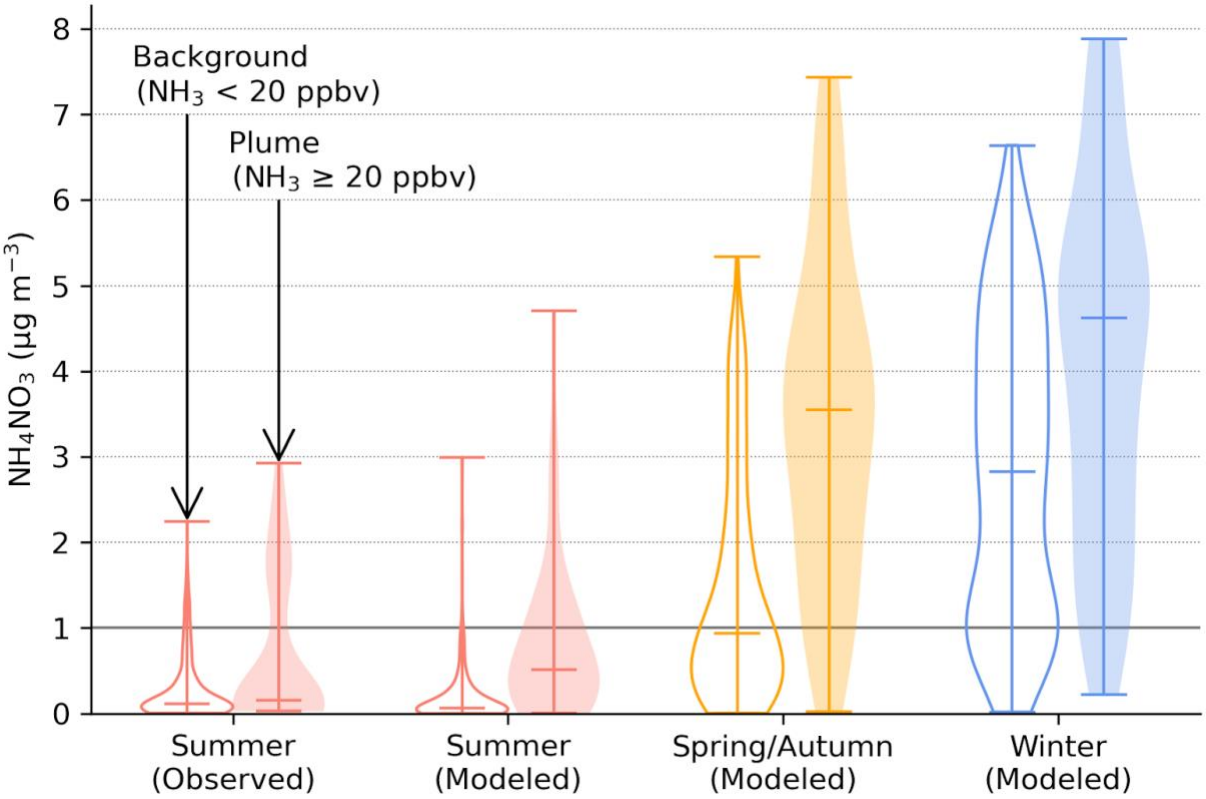

Figure S14. Violin plots of observed and modeled NH_4NO_3 by season (colors) for background (outline) and plumes (shading). Spring/autumn is modeled by perturbing the temperature in the model input by ΔT = -10˚C, and winter by ΔT = -20˚C.